공학박사학위논문

Dynamic Molecular Imaging of Living Cells in Tissue Regeneration

조직재생 추적을 위한
세포 분자 영상 기법

2019년 8월

서울대학교 대학원
협동과정 바이오엔지니어링 과정

박광리

Abstract

Dynamic Molecular Imaging of Living Cells in Tissue Regeneration

G. Kate Park

Interdisciplinary Program for Bioengineering

The Graduate School of Engineering

Seoul National University

Regenerative medicine holds immense potential for treating a wide range human disease, yet the mechanisms behind the therapeutic function of transplanted cells and biomaterials are not fully understood. Advances in molecular imaging have made it possible to quantitatively characterize damaged tissue, and they have allowed for the visualization of dynamic processes within a cell and even in the living body. Particularly, intraoperative optical imaging with monitoring the pathophysiological alteration of the target tissue/cell. However, a common set of challenges involving the development of targeted probes is the long-term detection of cell survival, differentiation, and integration with the host tissue for the early delineation of toxicity and function. In this study, we developed a novel fluorescent cell-labeling probe, CTNF126, in the near-infrared (NIR) window, which can be covalently fixed within the cells using

formalin or paraformaldehyde, while retaining high stability. Exploiting this technique to the next step, we achieved simultaneously monitoring of brain tissue regeneration and scaffold degradation in animal models using brain-specific NIR fluorophores, Ox1, in the 700 nm channel and ZW800-3a conjugated NIR hydrogel in the 800 nm channel. Taken together, these results highlight that the targeted imaging can be used as a promising platform for supporting therapeutic intervention and mechanistic insight in tissue regeneration.

Keyword : Optical Imaging, Near-infrared, Regenerative Medicine, Cell Tracking, Multichannel Imaging

Student Number : 2016-30276

Table of Contents

List of Tables

List of Figures

CHAPTER ONE: THE SCIENTIFIC BACKGROUND AND RESEARCH PROGRESS

1.1 Overview

Cell-based therapy involves administration of live cells or maturation of a specific cell population for the treatment of diseases: cardiac infarction, cancer, and tissue regeneration. The strategy involves isolating specific stem or immune cell populations from the patient for *ex vivo* modification. The cells are then administered into the host for the desired therapeutic effect, such as reprogramming of cells or inducing immune response. These modified cells in cell therapy are called effector cells and would potentially show a decrease in common side effects that arise from other treatments like chemotherapy. During modification, the effector cells are labeled *ex vivo* with imaging probes for tracking purposes. This imaging technique will play a crucial part in tailoring cell therapy as a personalized medicine by assessing the real time of cell localization, viability, and numbers (Fig 1.1).

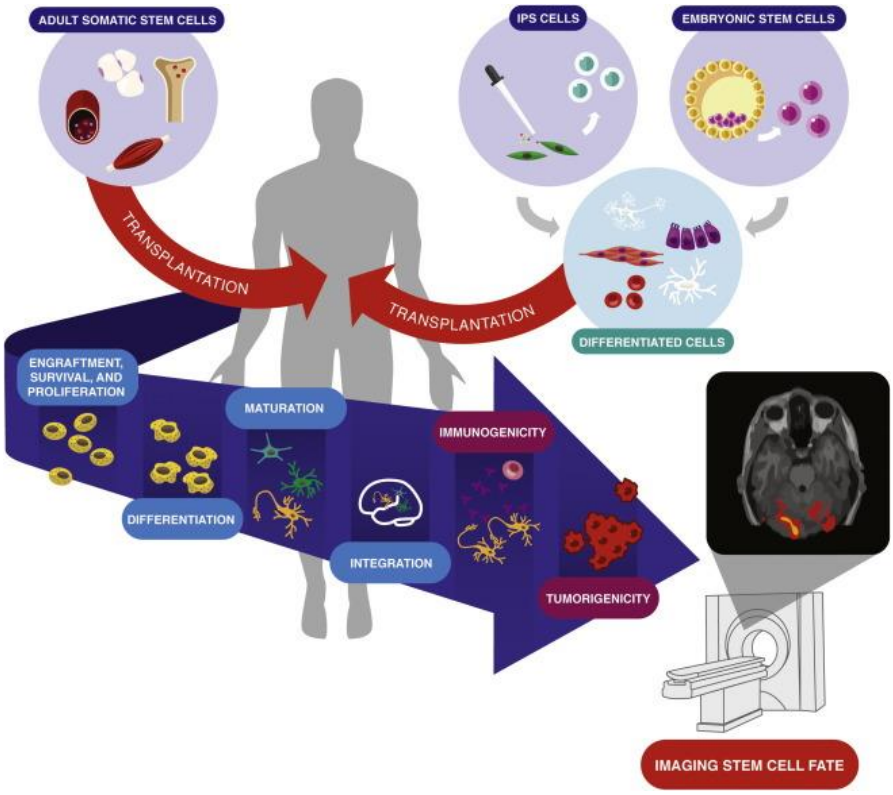

Figure 1.1 Stem cell-based therapy: Barriers to clinical translation. Current challenges in cell-based therapy are: 1) limited engraftment, survival, and proliferation, 2) poor differentiation, maturation, and integration, 3) immunogenicity with allogeneic transplantation, and 4) potential tumorigenicity with pluripotent stem cell derivatives. Molecular imaging will play a crucial role in overcoming these challenges and promote the clinical translation of cell-based therapy [1].

A better understanding of the fate of effector cells after transplantation will determine the successful implementation of cell therapy. Advances in molecular imaging have generated new opportunities to visualize and optimize the therapeutic efficacy of cell-based therapy by allowing longitudinal assessment of engrafted cell survival, integration, and proliferation. In order to monitor the transplanted stem cells with high resolution, there has been tremendous effort in developing techniques such as x-ray computed tomography (CT), magnetic resonance imaging (MRI), positron emission tomography (PET), and single-photon emission computed tomography (SPECT) [2]. However, these techniques are very costly, time consuming to implement, and generally restrained by the radioactive isotope's half-lives. Moreover, usage of radioisotopes is restricted as there is a limit for exposure due to toxicity. On the other hand, optical imaging is cost-effective, rapid, easy to use, non-ionizing, and can be readily applied. Therefore, improved and combined molecular imaging modalities will allow quantitative and qualitative trafficking of implanted cells in clinical trials (Fig 1.2). Capitalizing on the recent achievement in developing optical fluorescence imaging in cell-based therapy, we discuss the techniques including labeling methods and imaging probes and how these are applied to meet the criteria of high sensitive imaging for determining physiological behavior of cells during cell therapies.

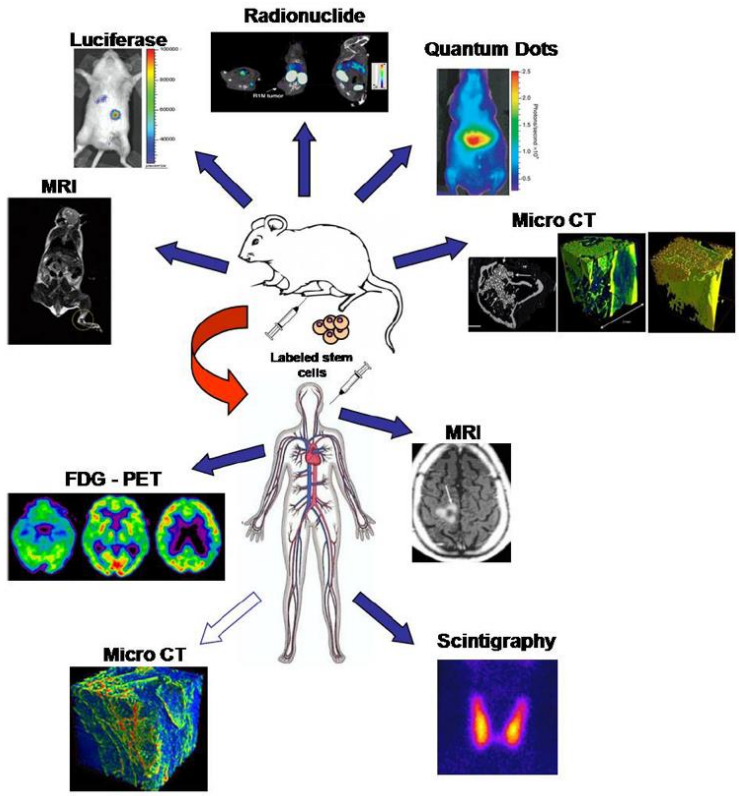

Figure 1.2 Recent advances in nanotechnology for stem cell tracking. Anatomical and *in vivo* molecular imaging used to assist researchers in locating labeled stem cell. MRI and radionuclide methods are also used in human studies.

1.2 Optical Fluorescence Imaging Probes

Optical fluorescence imaging of cell-based therapy is visualizing the fluorescence labeled cells non-invasively through an imaging system that can detect the fluorescence signal from its cellular milieu. The imaging system requires excitation light sources, appropriate emission filters, and a sensitive charge-coupled device (CCD) camera [3]. In addition, as cell based therapy is applicable in different parts of the body, the imaging system must be able to exclusively collect signals from the area of interest at the macroscopic level.

Optical fluorescence labeling involves introducing a fluorescent signal that enters the cell by active/passive transport and is trapped by intracellular materials [4]. There are two main labeling methods: 1) direct labeling with organic fluorescence dyes or quantum dots and, 2) indirect labeling by reporter gene/probe labeling. During direct labeling, contrast agent can bind to a certain targeted cell surface protein or be transported into the cell by diffusion, endocytosis, or active transport. This labeling is generally diluted with cell division and can result in errors of cell number quantification. For indirect labeling, cell transfection or transduction with reporter gene or probe is required and the labeling is retained after many divisions.

The imaging probes are crucial during optical fluorescence imaging as they are the key to identifying and developing the interactions

of the effector cells. Hence, imaging probes for cell therapy should have high specificity for tracking physiological fate of the transplanted cells. The sensitivity of detection is affected by the wavelength, quantum yield, and photo stability of the fluorophores. It is important that the probes must show no signs of cellular toxicity as well as systemic toxicity. In addition, cell labeling should not alter the function of effector cells when administered into the host. A number of optical fluorescence probes are currently available for cell-based therapy are shown in Figure 1.3.

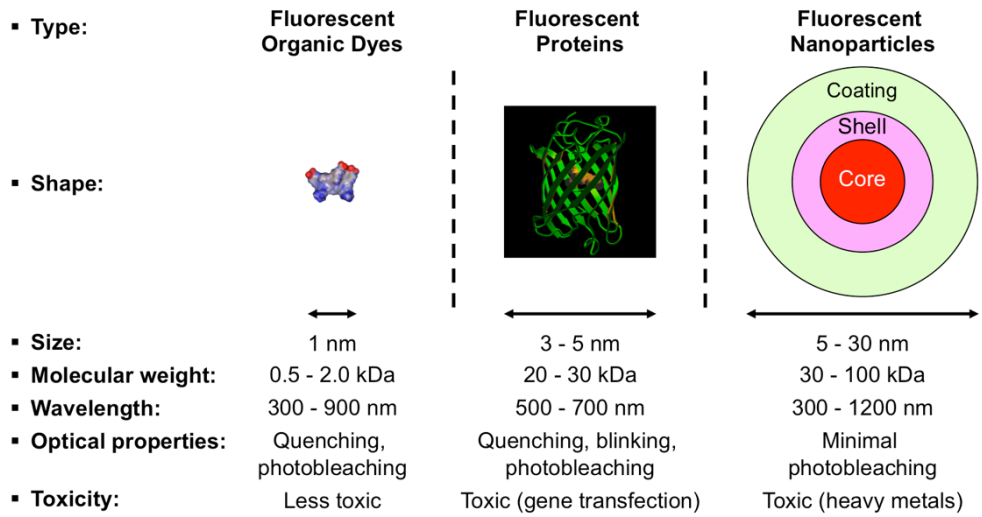

Figure 1.3 Comparison of fluorescent organic dyes, fluorescent proteins, and fluorescent nanoparticles [5].

1.3 Fluorescent Organic Dyes

The wavelength of fluorophores spans from UV (300-400 nm), visible spectrum (400-650 nm), and to the near-infrared (NIR) spectrum (650-900 nm) [2]. Many organic small molecules are commercially available for direct labeling such as Cy and Alexa dyes that can easily co-incubate with cells for short-term monitoring purposes since these dyes have no regeneration capacity and during cell division the signals will attenuate. For long-term labeling, chloromethylfluorescein diacetate dyes (Cell Tracker) and long chain carbocyanine dyes (DiL, DiO, DiD, and CM-DiI), have proven to be available [6]. Cyanine dyes, especially, can be utilized in imaging *in vivo* with target probes designed to visualize key components of the treatment area of cell-based therapy.

Cyanine combinations make super-resolution multicolor imaging possible. Of the combinations, Alexa Fluor, which is similar to Cy5, is thought to be the best performing. Cyanines can also be conjugated with ligands to target specific tumors. Recent researches focus to improve the photo-stability and brightness of cyanines.

1.4 Fluorescent Proteins

Currently, fluorescent proteins are one of the most frequently utilized fluorescent probes [7]. The first and most well-known is the green fluorescent protein (GFP) which was discovered and extracted from

jellyfish Aequorea victoria in 1962 by Shinomura et al. [8, 9]. Recently, fluorescent proteins with emitting longer photons, such as yellow fluorescent protein (YFP) and infrared fluorescent protein (IFP), were discovered in different species and extracted [10, 11].

The greatest advantage of fluorescent proteins is that these proteins can be genetically coded and labeled by one step. Fluorescent proteins are also helpful in studying cellular organelles, cells, and tissues because they are bright, photostable, and have low phototoxicity. Therefore they are widely used as probes. However, fluorescent protein is challenged by a variety of factors such as photostability, low quantum yield, larger size than OSMs and oligomerization that can cause cytotoxicity [2].

1.5 Fluorescent Nanoparticles

With the advancement of nanotechnology, several nanoparticles have developed in recent years [5, 12]. Organic and inorganic nanoparticles can be used to label cells with different labeling techniques such as surface chemistry and direct labeling via protein transporter or endocytosis (Fig 1.3). Organic nanoparticles have been diversely developed such as dendrimers, polymersomes, and liposomes [5]. An NIR dye Cy5 and vascular endothelial growth factor (VEGF) labeled boronated dendrimer was shown to bind to the upregulated VEGF receptors in

mouse breast carcinoma [6, 13].

Inorganic nanoparticles like small fluorescent quantum dots (QD) hold great promise to overcome the low sensitivity of FP to label cells with its outstanding brightness. QDs also have a broad wavelength (400–1200 nm) and high QY with symmetric narrow emission bands and high resistance to photobleaching indicating its photostability. Furthermore, they are versatile in their capability of bioconjugation [14]. By changing the surface chemistry, researchers can explore different biological applications. However, there exists the concern of toxicity to cells and dispersing in the cytosol because QDs are made of heavy metals (i.e. cadmium.) Currently, research is being conducted to overcome the limits of quantum dots such as Rao et al. who proposed a bioconjugate quantum dot that enhanced the sensitivity in small animal imaging [6].

1.6 Intraoperative Fluorescence Imaging Systems

Intraoperative fluorescence imaging systems are necessary for improving a surgeon's ability to visualize otherwise imperceptible anatomical structures [15]. The diversity of anatomical structures from patient to patient complicates identification, but fluorescence imaging systems and specific organ-targeting contrast agents allow surgeons to discern each structure on a case-by-case basis. The ideal intraoperative fluorescence imaging system should have a real-time overlay of white light and

fluorescence images, nanomolecular sensitivity, plausible utility during open surgeries, and the ability to simultaneously image multiple fluorophores [16]. Currently, most FDA-approved surgical imaging systems, such as the Hamamatsu Photodynamic Eye (PDE), Fluoptics Fluobeam 800, and Novadaq SPY are single- channel fluorescence video and image display systems [17, 18]. This proves disadvantageous since surgeons require an overlay of the fluorescent dye on a white light-guided image to properly identify pathological tissues and nearby anatomical structures. Additionally, PDE only provides screen captures, while the Novadaq SPY solely takes images when the target organ or tissue is exposed [16]. New NIR FLIs were developed to improve upon these limitations in intraoperative fluorescence image-guided surgery. Different forms of real-time imaging systems navigated by NIR fluorophores exist within FLI.

1.7 Multispectral Imaging Systems

The Fluorescence-Assisted Resection and Exploration (FLARE) imaging system produces an overlaid image of invisible NIR fluorescent light and color video, thus facilitating the identification of clear tumor margins and the avoidance of proximal tissues, nerves, and blood vessels during surgical procedures [17, 18]. FLARE consists of two separate NIR channels, two charge-coupled device (CCD) cameras (one for visual and

another for NIR), and dichroic mirrors that are used to focus light onto color video or NIR cameras [19]. The FLARE imaging platform (Fig. 1.4a) produces real-time color images and videos at wavelengths of 700 and 800 nm [3]. Color video and independent channels continuously acquire fluorescence images at rates up to 15 Hz over a 15 cm diameter field of view. The fluorescence of a region on organs or tissues are quantified using the custom FLARE software [20]. Different versions of FLARE systems such as the miniFLARE (Fig. 1.4b) and K-FLARE (Fig. 1.4c) employ two NIR fluorescence channels working simultaneously with color video, allowing the dual-channel imaging of various tissues with the appropriate fluorophores [21]. This is beneficial for observing and distinguishing nearby vasculature from critical anatomical structures and tumors during thoracic surgery.

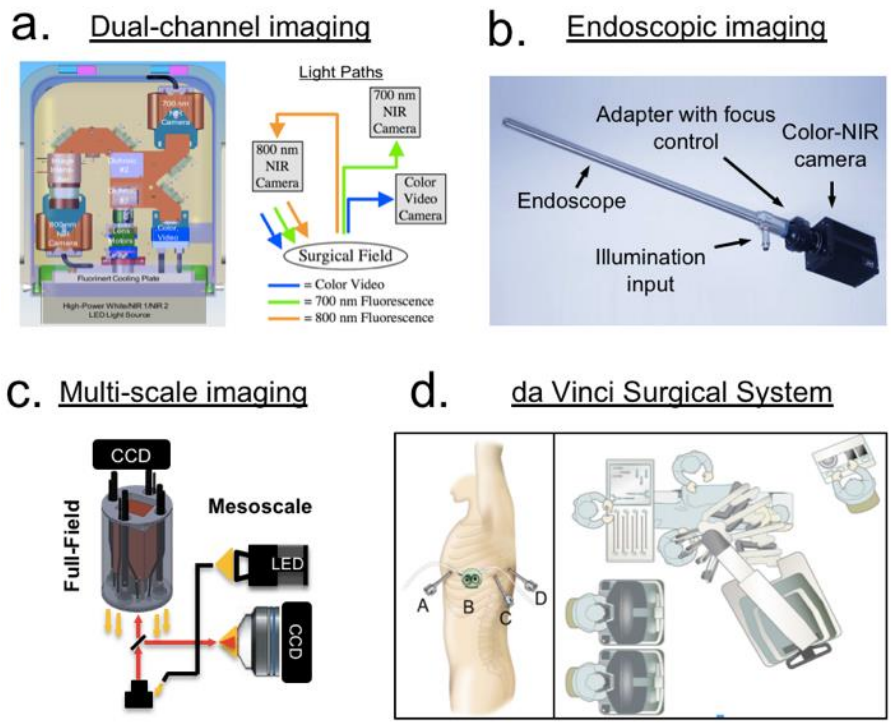

Figure 1.4 Intraoperative fluorescence imaging systems: (a) Dual-channel FLARE imaging system [19], (b) endoscopic imaging system [22], (c) multiscale multispectral imaging system [18], and (d) da Vinci Surgical System [23].

1.8 Optical Imaging in Cardiac Stem Cell Therapy

As cardiac disease is one of the leading causes of death globally, treatment for it is crucial. One of the treatments is cardiac stem cell therapy with injection of cells like skeletal myoblasts, bone marrow-derived cells, and cardiac resident stem cells. This treatment is aimed to repair acute or chronic damage to the myocardium. According to a number of studies, the transplant of stem and progenitor cells as the treatment cause direct or indirect therapeutic effects that prevent cell death, promote angiogenesis, and augment myocardial contractility. Stem cell therapy in the heart depends largely on the survival of transplanted cells; therefore, tracking the transplanted stem cell quantitatively and qualitatively is critical in cardiac stem cell therapy. This will further elucidate the molecular mechanisms of how the stem cells contribute to cardiac recovery [24].

Numerous studies have focused on monitoring the behavior of stem cells within the host cells using optical imaging (Fig 1.5). Hoshino et al. successfully labeled bone marrow-derived mesenchymal stem cells (MSCs) with an NIR fluorophore, IR-786. The labeled MSCs were observed *in vivo* for 90 minutes after intracoronary cells were injected into a myocardial infarction of a swine model [25].

Optical imaging has also been used to investigate the electrophysiological phenotype of MSCs in situ. MSCs are known to

improve cardiac electrophysiology in acute myocardial disorder, hence the optical imaging of cardiac electrophysiology of human induced pluripotent stem cell-derived cardiomyocyte (iPSC-CM)-based assays were investigated. NIR fluorescent voltage-sensitive dyes allowed high-precision in action potential measurements that markedly increased the throughput for electrophysiological characterization of human iPSC-CMs [26].

In another study, genetically encoded voltage indicators allowed assessing the cardiac excitation repeatedly with minimum invasion. With a cardiac myocyte-voltage-sensitive fluorescence protein 2.3 (VSFP2.3) monitoring the electric activity, function, and maturity in iPSC-derived cardiac myocytes was conducted [27].

Although many studies are investigating optical probes and imaging modalities suited for cardiac stem cell tracking, present studies show mostly of *ex vivo* and minimum invasive analysis. Optical imaging alone has limitations of noninvasive *in vivo* imaging because of the penetration depth and low sensitivity which needs improvement.

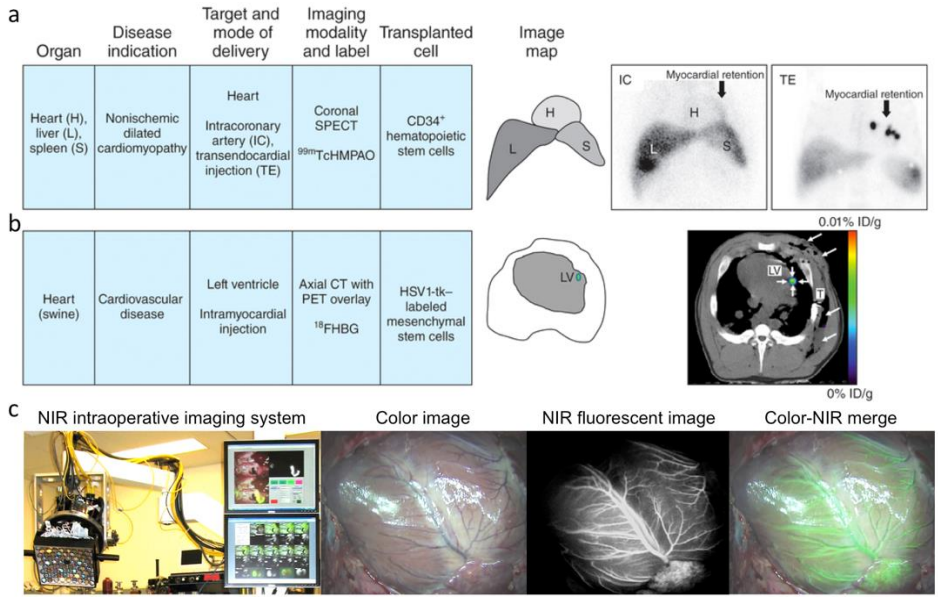

Figure 1.5 Clinical and preclinical imaging to track labeled cells in the heart: a) Coronal SPECT images of chest obtained after intracoronary (IC) versus transendocardial (TE) delivery of 99mTc-HMPAO CD34+ hematopoietic stem cells in patients. b) PET/CT fused axial multimodal imaging of swine. Adenovirus-transduced mesenchymal stem cells were implanted into porcine left ventricle (LV) myocardium after thoracotomy (long arrows). T is the chest tube inserted during surgery. 10^8 human MSCs injected into the myocardium were visualized (short arrows) 4 h after intravenous infusion. c) Real-time intraoperative optical imaging: NIR fluorophore-labeled bone marrow stem cells were injected into a swine model of myocardial infarction [28].

1.9 Optical Imaging in Tissue Regeneration

Tissue engineering focuses on *in vitro* repair of tissues and/or organs to restore or regenerate the function of damaged organs by using appropriate scaffolds and cell sources [29, 30]. The potential of stem cells to differentiate into bone, fat, cartilage, and muscle cells has shed light on cell-based tissue regenerative medicine to treat critical conditions such as osteoarthritis, osteoporosis, and spinal injury [31]. For successful tissue regeneration, a suitable biocompatible scaffold should provide an optimal environment for tissue formation [32]. Also, the rate of scaffold degradation and tissue formation should generally be equivalent. Therefore, accurate and longitudinal measurements of these changes play the key role in tissue engineering and regenerative medicine. However, current analytical methods such as histological and microscopic analyses are mostly invasive and demand multiple samples, which result in batch-to-batch variations and thus inaccurate conclusions.

Advanced optical imaging outperformed the traditional imaging methods by providing longitudinal noninvasive information on tissue constructs. Artzi et al. studied *in vitro* and *in vivo* tracking of biodegradable hydrogels conjugated with low wavelength fluorophores, such as fluorescin (λem 512 nm) and Texas red (λem 615nm) [33]. They proposed a dual exponential decay model to quantitatively correlate the *in vitro* biodegradation pattern to the obtained *in vivo* animal data.

However, this is rather complicated due to endogenous tissue autofluorescence in the visible wavelength range and physiochemical instability in the body, which conflicts the visible dyes with the erosion rate. To overcome these limitations, NIR fluorophores have been used to monitor *in vitro* and *in vivo* scaffold degradation because of their long-term stability, reduced background signals, and higher sensitivity compared to visible fluorophores.

Kim et al. implanted collagen scaffolds labeled with zwitterionic heptamethine indocyanine ZW800-1 (λem 780 nm) in living animals [34]. By introducing invisible NIR fluorescent light, the long-term scaffold degradation profile was successfully achieved in the same animal over 35 days and no endogenous interference was observed. Although promising contributions of NIR fluorophores in detection of scaffold degradation *in vivo* have been made, the noninvasive application is limited to imaging superficial tissues and organs such a skin, muscle, cartilage, bone, eye (vasculature), and white/brown adipose tissue because of its intrinsic optical scattering.

To monitor deeper tissues or inside organs, minimal-invasive (using endoscope) or invasive surgical procedures are required. In addition, a single imaging modality is limited by various chemical, mechanical, biological, and physiological factors. Therefore, it is essential to adapt multimodal imaging techniques such as ultrasound, MRI, SPECT,

PET, and micro-CT for better understanding of tissue regeneration processes. These multiple potentials of this field are applicable to cell based tissue regeneration therapy.

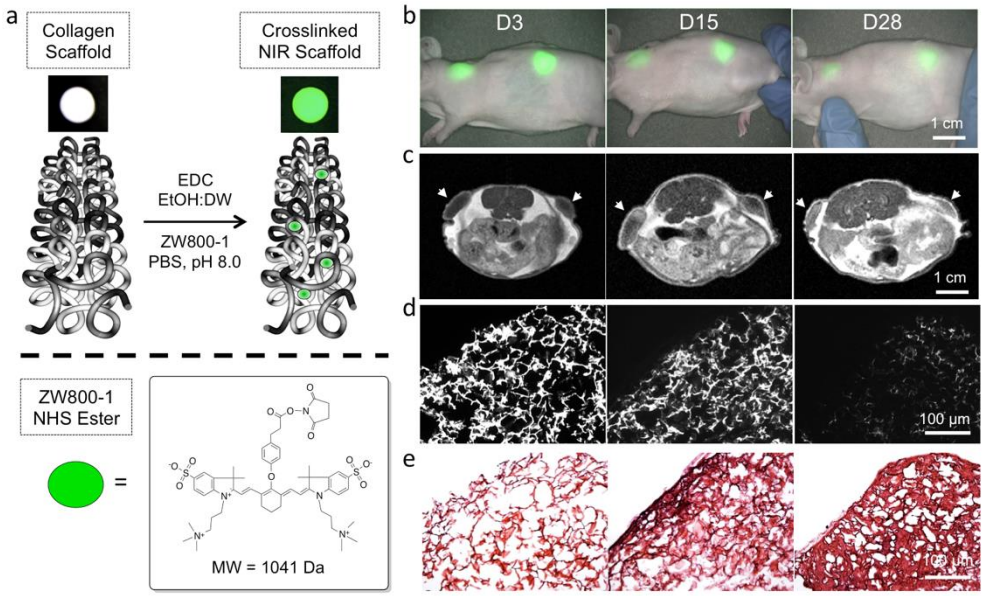

Figure 1.6 Optical and MR imaging for tracking tissue regeneration. a) NIR fluorophore-conjugated collagen scaffold. b,d) Quantification of *in vivo* scaffold degradation in nude mice by optical fluorescence imaging. c,e) Quantification of *in vivo* tissue regeneration in nude mice by MR imaging and H&E histological evaluations [35].

1.10 Summary

Cell-based therapy holds great potential to treat countless human diseases. However, the mechanisms responsible for cell migration and homing are not elucidated yet, and the possible structural and functional outcomes of cell transplantation for disease treatment are under investigated. Nonetheless, noninvasive imaging of administered cells with radioisotopes or optical fluorescence is a prerequisite to evaluate the therapeutic efficacy of cell-based therapy [36]. Additionally, *in vivo* optical imaging can be used to improve the current barriers to determine the physiological behaviors of cells after successful transplantation. This work focuses on various imaging modalities, such as nuclear imaging, magnetic resonance imaging, and optical fluorescence imaging, for tracking cells prelabeled with imaging probes in the body. Of particular focus of this review is on how optical imaging has advanced the treatment of cardiovascular diseases, and tissue regeneration through the cell-based therapy.

CHAPTER TWO: LYSOSOME-TARGETED BIOPROBES FOR SEQUENTIAL CELL TRACKING FROM MACROSCOPIC TO MICROSCOPIC SCALES

2.1 Introduction

Recent advances in molecular imaging have provided insight for the *in vivo* behavior of transferred cells, aiding in both preclinical and clinical studies [1, 28, 37]. To extract data of biological function and activity from a single cell or from a population of cells, comprehensive and sequential imaging analysis from *in vivo* tracking to *ex vivo* pathophysiology is critical. However, it has been difficult to use fluorescence imaging techniques to visualize both the biological behavior of contrast agents in the body and molecular based consequences simultaneously because of the sensitivity of staining influenced by washing, fixation, and permeabilization on retention of fluorescence signal [38]. Therefore, it is important to improve the capability of tracers for real-time *in vivo* and *ex vivo* post-analysis in terms of binding specificity and chemical properties for better diagnostic interpretation.

General strategies for efficient biological imaging include the use of organic dyes [39], inorganic nanoparticles [40], and fluorescent proteins [41]. However, these often suffer from cytotoxicity and photobleaching as well as leakage of tracers and engulfment by

neighboring cells, resulting in false-positives. Transfection of cells with fluorescent proteins, such as green fluorescent protein (GFP), allows longitudinal tracking of *in vivo* cell proliferation, but it can be difficult to reach the fluorescence density required for imaging cells in a short period of time [42, 43]. To overcome these problems, different types of lipophilic organic fluorescent bioprobes have been developed to label subcellular components, such as cell membranes, lysosomes, and mitochondria [44]. However, tagging membrane can interfere with cellular mobility, and staining mitochondria can affect the membrane potential changes [45]. Lysosomes are digestive organelles with active endocytosis that absorb biomolecules to provide nutrition to the cells or degrade pathogens to protect the cells [46]. Therefore, staining lysosomes for the purpose of tracing cells can minimize potential alterations to the cellular activities.

We focused on the design of fixable bioprobes to target lysosomes and trap inside the lysosomal membrane to eliminate efflux and washout after staining the cells. Frist, we developed heptamethine near-infrared (NIR) fluorophores for cellular tracking in living organisms (Fig 2.1) because the NIR window (650-900 nm) is advantageous for bioimaging due to low tissue absorbance, low tissue scattering, and low autofluorescence compared with UV-visible region [15].

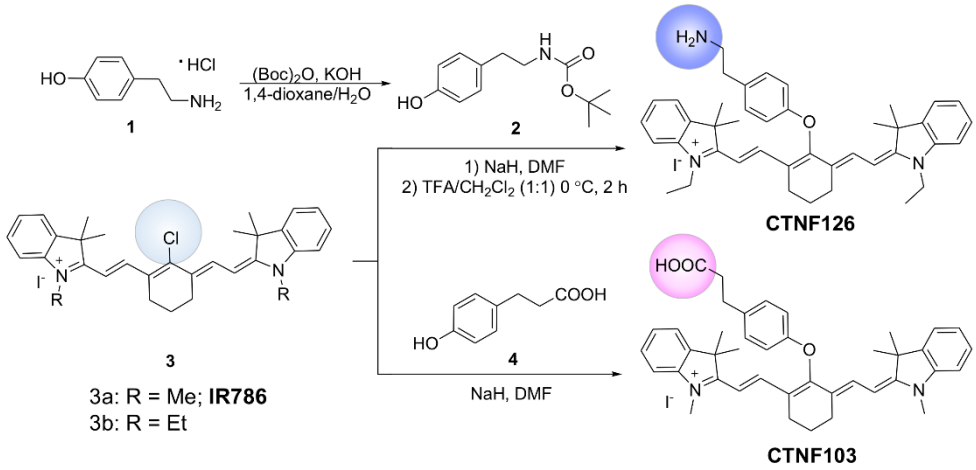

Figure 2.1 Synthetic scheme for CTNF126 and CTNF103.

2.2 Materials and methods

2.2.1 Chemicals and syntheses

All chemicals and solvents were of American Chemical Society grade or HPLC purity. All chemicals were purchased from Fisher Scientific (Pittsburgh, PA), Sigma-Aldrich (Saint Louis, MO), and Acros Organics (Pittsburgh, PA), unless noted otherwise. LysoTracker™ was obtained from Molecular Probes (Eugene, OR), and IR786 was purchased from Sigma-Aldrich. For synthesis of CTNF126 and CTNF103, heptamethine fluorophores were synthesized first, and they were assorted with side groups. Chloro-substituted dyes were synthesized as previously reported, through salt condensation with Vilsmeier-Haack reagent to build the heptamethine cyanine core [47-50]. Then, substitution of different ionizable docking functional groups (phenoxide ions) were made on the meso-chlorine atom of the heptamethine cyanine core to compare selective cellular retention of each fluorophore and further docking in the subcellular component (Scheme S1). The final compounds were analyzed by ^{1}H NMR, ^{13}C NMR, and HRMS.

2.2.2 Measurement of optical properties

Absorbance and fluorescence were measured using fiberoptic HR2000 (200−1100 nm) spectrometers (Ocean Optics, Dunedin, FL). Fluorescence excitation was provided by a 5 mW, 655 nm laser diode (Opcom Inc., Xiamen, China) coupled through a 300 mm core diameter, NA 0.22 fiber (Fiberguide Industries, Stirling, NJ). All optical measurements were made in serum−containing media. 5 μM of each fluorophore solution was prepared in 10% FBS solutions and incubated at 37 ℃ for 4 h to evaluate their photostability and physicochemical stability. In silico calculations of physicochemical properties such as molecular weight, charge, distribution coefficient (logD at pH 7.4), pKa, refractivity, topological polar surface area (TPSA), H−bond donors/acceptors, and rotatable bonds were calculated using JChem calculator plugins (ChemAxon, Budapest, Hungary). Data plotting was performed using Prism version 4.0a software (GraphPad, San Diego, CA) and Microsoft Excel (Redmond, WA).

2.2.3 Live cell labeling and *in vitro* imaging

Human prostate cancer cells (PC3 cells) were seeded into 24−well plates (5×10^4 cells per well) and incubated at 37 ℃ in humidified 5% CO_2 incubator in DMEM containing 10% fetal bovine serum (FBS)

and 1% penicillin streptomycin for 2 days. After washing twice with media solution, CTNF126, IR786, and CTNF103 were added to each well at a concentration of 2 μM and incubated for 30 min at 37 ℃. To improve image contrast, cells were washed three times with media solution prior to imaging. The images were acquired either right after the triple wash, or right after additional washing with 1% Tween 20 to compare fluorescent signal reduction among the contrast agents. The live cell imaging was performed using Nikon TE2000 epifluorescence microscope equipped with a 75W Xenon light source and an Orca-ER (Hamamatsu, Bridgewater, NJ) camera. The filter set (Chroma Technology Corporation, Brattleboro, VT) composed of 710±25 nm excitation filter, 785 dichroic mirror, and 810±20 nm emission filter was used to detect all NIR fluorophores. These cells were observed again after 2 days to compare long-term stability.

2.2.4 *In vivo* cell tracking and histological analysis

Animals were housed in an AAALAC-certified facility and were studied under the supervision of BIDMC IACUC in accordance with the approved institutional protocol (#057-2014). 6-week-old C57BL/6 mice (male; 20-25 g) were purchased from Charles River Laboratories (Wilmington, MA). Animals were anesthetized with

100 mg/kg ketamine and 10 mg/kg xylazine intraperitoneally (Webster Veterinary, Fort Devens, MA). B16F10 cells were stained with 2 μM of CTNF126 or IR786 for 30 min at 37 ℃, and detached with cell scraper. 1×10^6 cells per mouse were injected intravenously into the mice. Animals were sacrificed 5 min and 24 h post-injection of the cells, respectively.

The lung cavity was opened to observe injected cells in the lung using our custom-built intraoperative NIR imaging system, which equipped 760 nm excitation light (3.6 mWcm-2) and white light (400-650 nm) at 5500 lux. Color and NIR fluorescence images were acquired simultaneously with custom software at rates of up to 15 Hz over a field of view with a diameter of 15 cm. The lungs were resected and embedded in Tissue-Tek O.C.T. compound (Sakura Fineteck, Torrance, CA).

The tissues were then cryosectioned at 10 μm interval and stained with hematoxylin and eosin (H&E) for further visualization with the customized TE2000 NIR fluorescence microscope. For validation of fluorescent signal retention during histological analysis, we preceded a standard method using cell pellets. PC3 pellets were seeded onto 100 x 15 mm petri dishes and incubated at 37 ℃ in humidified 5% CO_2 incubator in the media solution until the cell confluency reached 90%. 1×10^7 cells (~ 5 petri dishes) were

stained with CTNF126 or IR786 at a concentration of 2 μM and incubated for 30 min at 37 ℃. After washing with media solution, the cells were collected using cell scraper and centrifuged at 1200 rpm for 10 min. After the same histological preparation was conducted, the sectioned slides were imaged using the microscope using 20X objective.

2.2.5 Quantitation and Statistical Analysis

Fluorescent intensity (FI) of a region of interest (ROI) over various tissues was quantified using Image J software (NIH, Bethesda, MD). Signal-to-background ratio (SBR) is FI of ROI / background (BG) intensity. Results were presented as mean (n = 5) ± standard deviation (s.d.). Statistical analysis was performed using a one-way ANOVA between multiple groups. A P value of less than 0.05 was considered significant (*P <0.05; **P <0.01; ***P <0.001).

2.3 Results and Discussion

2.3.1 Synthesis of Cell Tracking Fluorophores

A series of ionizable docking functional groups were substituted to the heptamethine cyanine imaging core to compare selective cellular retention and further docking in the subcellular component. Chloride (−Cl), carboxylate (−COOH), primary amine (−NH2), and secondary amine (−NH−) were introduced as a pendant domain on the mesocarbon of the heptamethine backbone (Fig. 2.2−2.5). Chloro−substituted fluorophores were synthesized through salt condensation with Vilsmeier−Haack reagent to build the polymethine cyanine core (Scheme S1), and the phenoxide ions were conjugated to the meso−chlorine atom through the SRN1 displacement pathway. Because the protonated oxygen exhibits limited nucleophilicity, NaH was used to generate the phenoxide ion in situ. For the synthesis of fluorophore with a primary amine docking group (CTNF126), we initially protected tyramine hydrochloride using the Boc−group to ensure selective reactivity at the oxygen atom (Fig. 2.6a). After conjugation of the tyramine on the heptamethine cyanine, the Boc protection was removed to form the final structure of CTNF126.

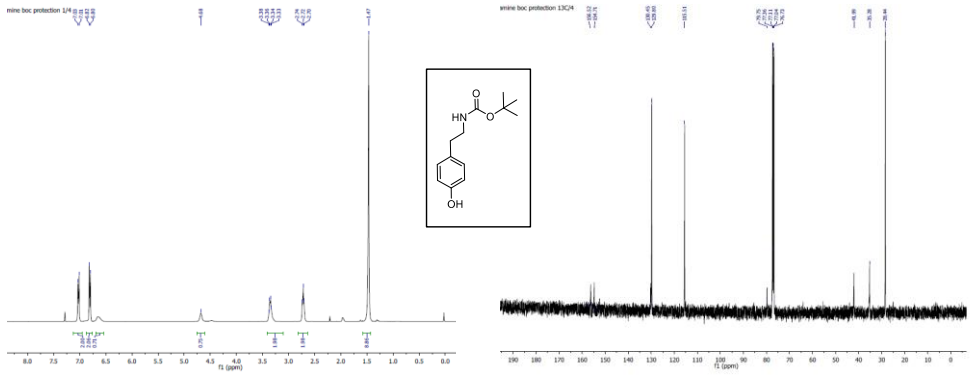

Figure 2.2. ^{1}H and ^{13}C NMR spectra of Compound 2.

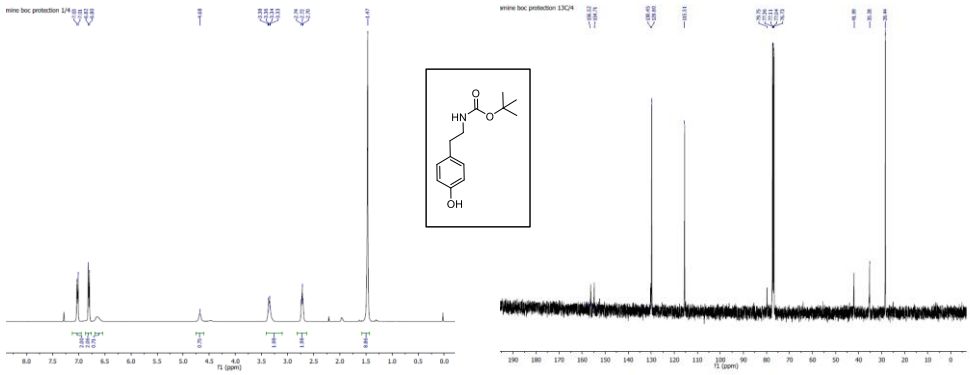

Figure 2.3. ^{1}H and ^{13}C NMR spectra of CTNF126.

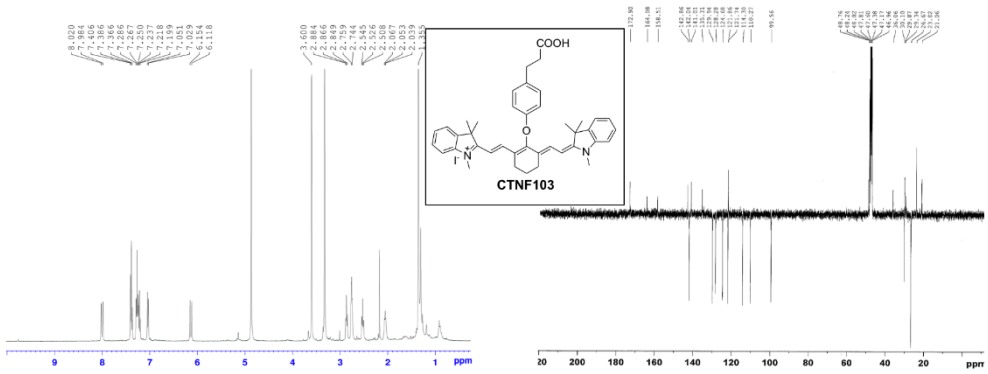

Figure 2.4. ^{1}H and ^{13}C NMR spectra of CTNF103.

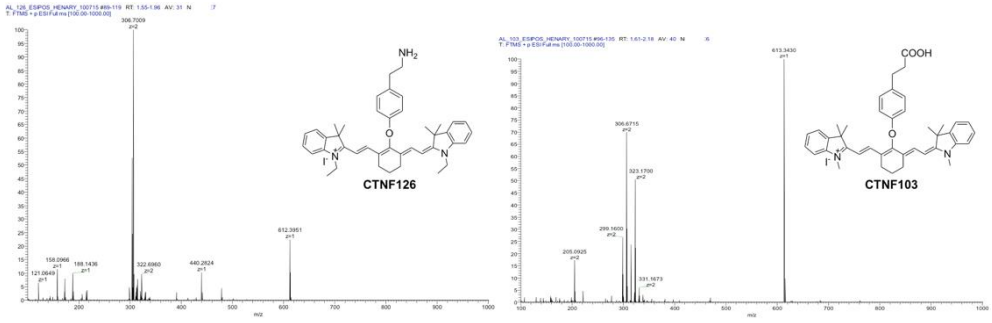

Figure 2.5. HPLC-MS analysis for CTNF126 and CTNF103.

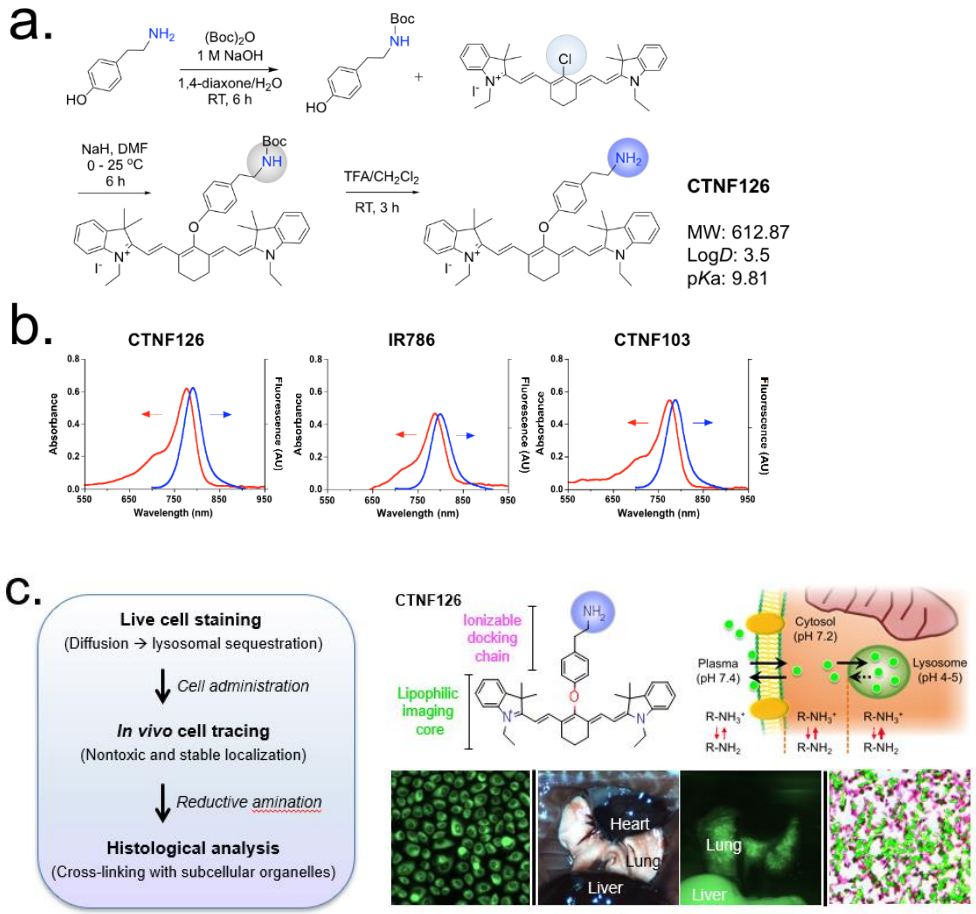

Figure 2.6. Design of lysosome-targeted NIR fluorophores: (a) Synthetic scheme of CTNF126 composed of two functional groups and (b) optical properties of three representative NIR fluorophores. Absorbance (Abs) and fluorescence (Fl) spectra were measured in FBS at 5 μM. (c) Longitudinal cell tracking process of NIR fluorophores and lysosomal sequestration of CTNF126. A thickness of red arrow represents ionization tendency.

2.3.2 Physicochemical and optical properties of CTNFs

Comparative absorption and fluorescence emission spectra were recorded for newly synthesized fluorophores, CTNF126, IR785, and CTNF103, and all showed stable optical properties in the NIR window (Fig. 1b). Table 1 summarizes the physiochemical and optical properties of newly synthesized NIR fluorophores. Extinction coefficient and fluorescence quantum yield values for all three were similar (ε >110,000 $M^{-1}cm^{-1}$; Φ > 23). However, CTNF126 has the highest molecular brightness in serum-containing media (44,660 $M^{-1}cm^{-1}$). In addition, all three fluorophores are lipophilic cations (logD > 3.0 at pH 7.4) which can readily diffuse across cell membrane by passive diffusion. However, only CTNF126 can becomes protonated (pKa > 6.0) in the acidic environment of lysosome (pH 4-5) [51]. This shifts the equilibrium, favoring the ionized form that could limit the diffusion of CTNF126 back across the lysosomal membrane into the cytosolic space [52]. As a result, the protonated CTNF126 is retained inside the cell, which is necessary for bioprobe to be an inert cell tracer with enhanced photo-activity.

Physicochemical property	CTNF126	IR786	CTNF103
Formula	$C_{42}H_{50}N_3O$	$C_{32}H_{36}ClN_2$	$C_{41}H_{45}N_2O_3$
Molecular weight (Da)	612.87	484.09	613.81
LogD at pH 7.4	3.5	4.79	6.54
Total charges at pH 7.4	1	1	0
p*Ka*, strongest basic	9.81	1.92	4.05
Topological polar surface area (Å^2)	41.5	6.25	52.78
Hydrogen bonding acceptor(s)	3	1	7
Hydrogen bonding donor(s)	1	0	1
Optical property in media	**CTNF126**	**IR786**	**CTNF103**
Absorbance maximum (λ_{abs}, nm)	778	786	773
Emission maximum (λ_{em}, nm)	790	800	786
Stokes shift (nm)	12	14	13
Extinction coefficient (ε, $M^{-1}cm^{-1}$)	154,000	117,500	137,500
Quantum yield at 770nm (Φ, %)	29.0	23.0	29.0
Molecular brightness ($M^{-1}cm^{-1}$)	44,660	27,025	39,825

Table 1. Physicochemical and optical properties of lipophilic NIR fluorescent fluorophores.

2.3.3 Lysosome-Targeted Bioprobes for Sequential Cell Tracking

Figure 2.6c summarizes an innovative design of CTNF126 with two functional domains for ionizable docking and lipophilic imaging, respectively, that allows for avoidance of physical or biochemical interference of NIR bioprobes with cellular activities. The heptamethine cyanine core is used for the sequential imaging with high photostability and serum stability from *in vivo* to *ex vivo* using the FLARE imaging system [47, 49]. Sufficient photostability in biological media is another essential property for prolonged live cell imaging [39, 53]. As shown in Fig 2.7, the photostability of CTNF126 was determined in warm serum, where all three fluorophores showed over 95% serum stability during 4 h post-incubation. Additionally, the structure provides appropriate lipophilicity allowing it to penetrate inside the live cell membrane. Rapid passive diffusion into the cell can be followed by selective lysosomal sequestration, and the fluorophores could be trapped inside the cells. Furthermore, the fixable property of CTNF126 allows retention in the tissue after resection and chemical treatment for histological analysis.

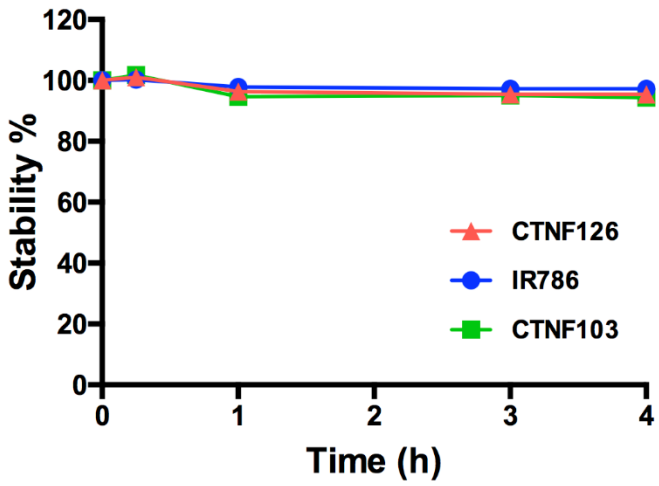

Figure 2.7 Photostability and physicochemical stability of CTNF126, IR786, and CTNF103. 5 μM of each fluorophore was incubated in fetal bovine serum (FBS) supplemented with 50 mM HEPES (pH 7.4) at 37 °C for 4 h.

2.3.4 *In vitro* stability test of CTNFs

To compare the cellular permeability and retention, CTNF126, IR786, and CTNF103 were loaded into living PC3 cells individually, and their cellular behaviors were compared in various conditions (Fig 2.8). All three lipophilic cations achieved saturation of loading into cells within 10 min, and with extracellular concentrations ranged from 0.5 to 10 μM. At these high concentrations, the tested fluorophores did not exhibit any evidence of toxicity. In particular, no observed change in cellular morphology was observed, and neither was a decrease or increase in the rate of proliferation nor a change in cell plating efficiency. In addition, the strong signal strength of CTNF126 was maintained in active proliferation of the cells after an additional 24 h incubation, while cells stained with IR786 and CTNF103 had virtually no intracellular retention signals due to the efflux of fluorophores (Figure 2.8a). To show that CTNF126 is fixable, the cells were treated with 4% formaldehyde after staining and washed with 1% Tween 20 (Fig. 2.8b). Despite potential interaction of the chloride atom of IR786 with intracellular proteins, significantly reduced signal was observed after fixation and detergent washing (***$P < 0.05$ for IR786; ***$P < 0.001$ for CTNF103) [54]. CTNF126, however, is fixed in place with no loss of signal after detergent washing. CTNF126 demonstrated high efficiency and rapid loading into live cells (Fig. 2.9), as well as exhibited excellent partitioning behavior and retention.

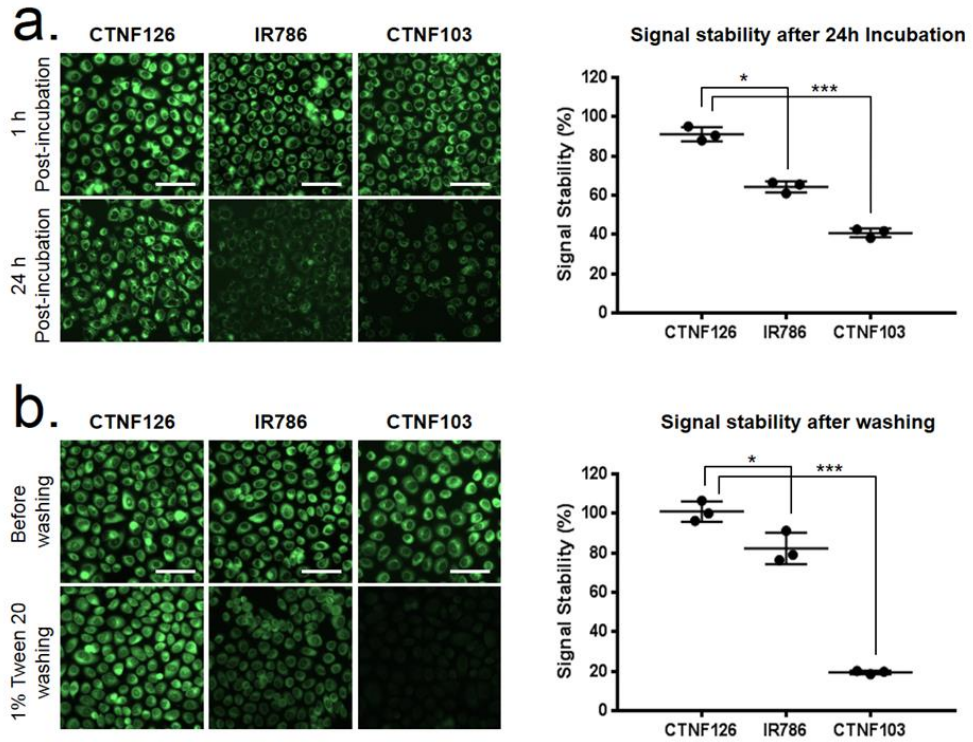

Figure 2.8 Physicochemical and optical stability of lysosome-targeted NIR fluorophores: (a) Long-term cellular stability of CTNF126, IR786, and CTNF103 in live PC3 cells and (b) their stability after formaldehyde fixation and detergent washing was calculated (n = 5, mean ± s.d., *P <0.05; ***P <0.001). Scale bars = 25 μm.

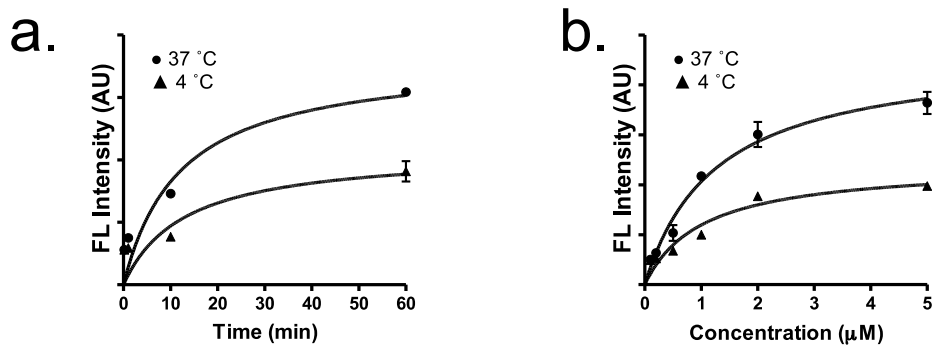

Figure 2.9 *In vitro* cellular uptake of CTNF126 in PC3 cells with various incubation times (a) and concentrations (b).

2.3.5 *In vivo* stability test of CTNFs

To validate direct translation of CTNF126 for *in vivo* cell tracking, 1×10^6 PC3 cells stained with either CTNF126 or IR786 were suspended in the media solution and administered into syngeneic C57BL/6J mice intravenously. The mice were sacrificed at 5 min and 24 h post-injection, and the thoracic cavity was opened and imaged under real-time image guidance using the intraoperative optical imaging system (Fig. 2.10a). At an initial deposition, the cells with both CTNF126 and IR786 showed similar signal intensity from the lungs. However, after 24 h, only the cells stained with CTNF126 could be observed in the lungs. The signal intensity of the lung was attenuated at 24 h due to migration of the cells from the lung capillaries to the liver, which was traceable (i.e., increase in liver signal) [5]. This *in vivo* cell tracking was emphasized by changing the injection method. As shown in Figure 2.8b, the cells orthotopically injected into the liver were found in the lung 6 h post-injection, which implies migration of the cells through hepatic vasculatures. NIR *in vivo* fluorescence imaging confirmed that prolonged lysosome sequestration of CTNF126 is the key to real-time visualization of tracing administrated cells. This mechanism differs from other lysosomal targeting and pH-sensitive probes where their purpose is to monitor metabolic cellular activities. In this case, bioprobes are effluxed from the targeted organelle in 1-2 h.

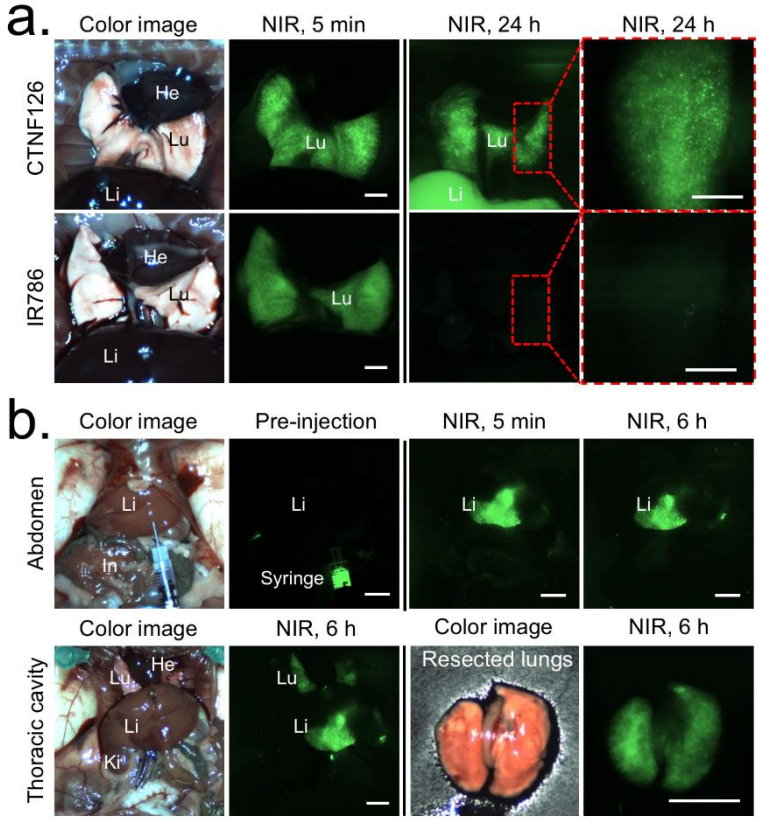

Figure 2.10 *In vivo* tracking of lysosomal fluorophore-labeled cells using the intraoperative optical imaging system. (a) CTNF126 and IR786-stained cells were trapped in the lung with strong fluorescent signal at 5 min post-intravenous injection. The cells labeled with CTNF126 were found in the liver as an evidence of cell migration from the lung capillaries at 24 h post-injection. (b) The cells injected into the liver orthotopically were found in the lung after 6 h, implicated liver-to-lung trafficking of the cells. All NIR fluorescence images are identically normalized. Abbreviations used are: He, heart; In, intestine; Ki, kidney; Li, liver; Lu, lung. Scale bars = 3 mm.

2.3.6 Fixable Properties of CTNF126

One of the major challenges of fluorescence imaging in real-time cell tracking is insufficient thermal and biological stability of fluorophores, which limit continuous recording of the fate of cells after administration of stained cells [35]. Hematoxylin and eosin (H&E) is the gold standard for analyzing biopsy specimens in clinics, and cell tracking technology must be compatible to make a significant impact in the field [55]. However, H&E processing is extremely harsh, requiring exposure to high temperature of at least 58 ° C for over 1 h and exposure to other organic solvents as strong as xylene during the tissue embedding and staining processes. There are currently no fixable cell-tracking NIR bioprobes that can withstand these punitive conditions [38]. CTNF126 is designed to be fixed covalently within the cell using formalin or paraformaldehyde by forming a cross-link methylene bridge, while retaining high stability [56]. To prove this, the same human tissue biopsy procedure used clinically was performed using cell pellets and lung tissue samples (Fig. 2.10). First, 1×10^7 PC3 cells stained with either CTNF126 or IR786 were collected using cell scraper and centrifuged at 1200 rpm for 10 min. The cell pellets were prepared into a paraffin block (Fig. 2.12) and underwent histological staining to evaluate the fluorescence retention or attenuation. As shown in Figure 2.11a, IR786 largely washed away during histological processing while CTNF126 was fixed in place and withstood

high temperature and organic solvent washing. Next, the lung tissues were harvested after intravenous administration of the stained cells and performed the cryosection at a thickness of 10 μm followed by H&E staining. As expected, CTNF126 was resistant to the harsh processing and allowed further visualization of the cells while IR786 was mostly washed out from the stained cells localized in the lung tissue (Fig. 2.11b). This makes it possible to combine NIR fluorescence and H&E staining of the same slide, thus allowing us to locate a single cell on an H&E stained tissue slice while co-staining for differentiation markers [57].

To confirm the location of cellular uptake, PC3 cells were labeled with a series of NIR fluorophores. At 2 μM concentration, IR786 and CTNF103 were found in the mitochondria (data not shown) [58], while CTNF126 targeted lysosomes confirmed by co-registration with LysoTracker (Fig. 2.11c). It is well known that lipophilic cations exhibit differential subcellular localization depending on concentrations: mitochondria uptake at low concentrations and endoplasmic reticulum (ER) accumulation at higher concentrations [59, 60]. Next, to prove photostability in cells, CTNF126 and LysoTracker were dissolved in 100% serum at a concentration of 2 μM and incubated at 37 °C over 24 h (Fig. 2.13a). CTNF126 was stable in warm serum over the period of incubation (> 99%) without biological/chemical degradation (biodegradation) nor photo-induced degradation (photobleaching). Finally, the biological

stability of CTNF126 was evaluated in PC3 cells, where CTNF126 showed significantly higher photostability compared with LysoTracker after 24 h incubation (Fig. 2.13b; n = 5, mean ± s.d., **P <0.01). This proves that CTNF126 is fixable inside lysosomes, which limits efflux elimination and stabilizes in the cell without degradation.

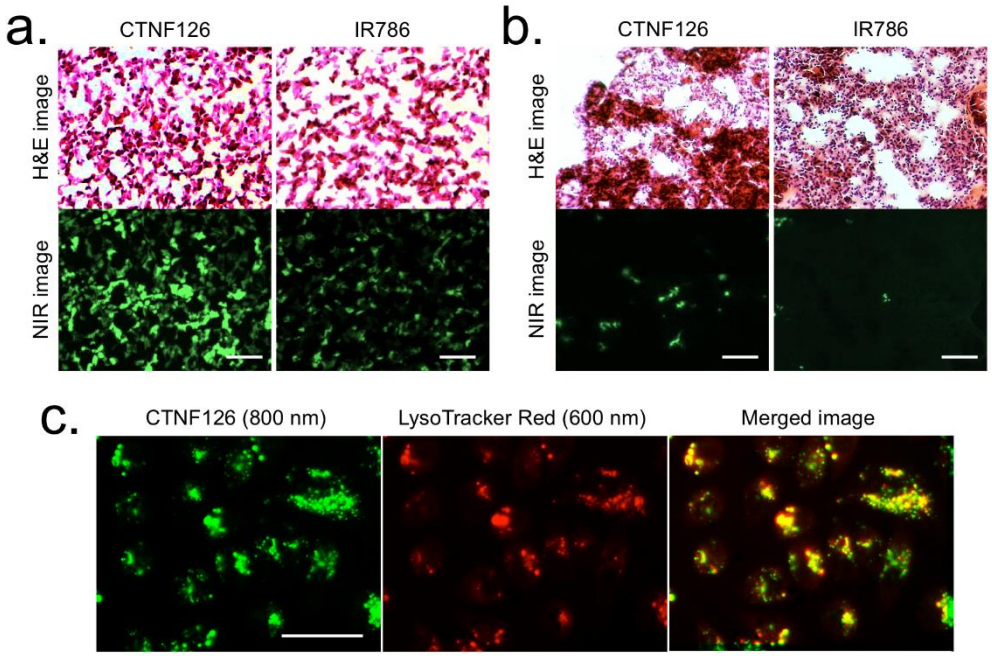

Figure 2.11 Stability of histological processes, including formaldehyde fixation and H&E staining: (a) Cell pellets mimicking the tissue structure and (b) the lung tissue sections harvested from C57BL/6 mice after intravenous administration of the cells labeled with lysosomal-targeted fluorophores. (c) Lysosomal sequestration of CTNF126 (left), LysoTracker (middle), and merged image of the two (right) in PC3 cells. All NIR fluorescence images have identical exposure and normalization. Scale bars = 25 μm.

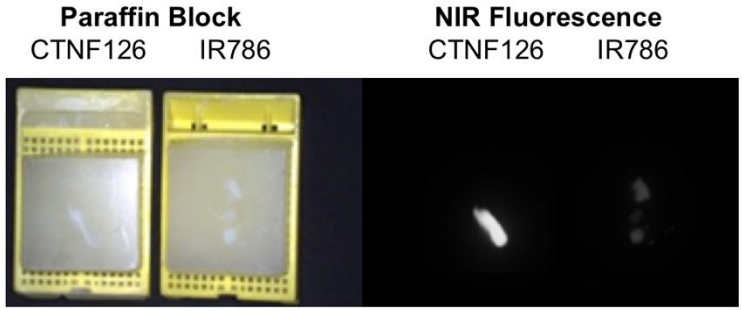

Figure 2.12 Thermal stability of CTNF126 and IR786. Each NIR fluorophore-labeled PC3 cell pellets were processed into a paraffin block and imaged under the NIR imaging system.

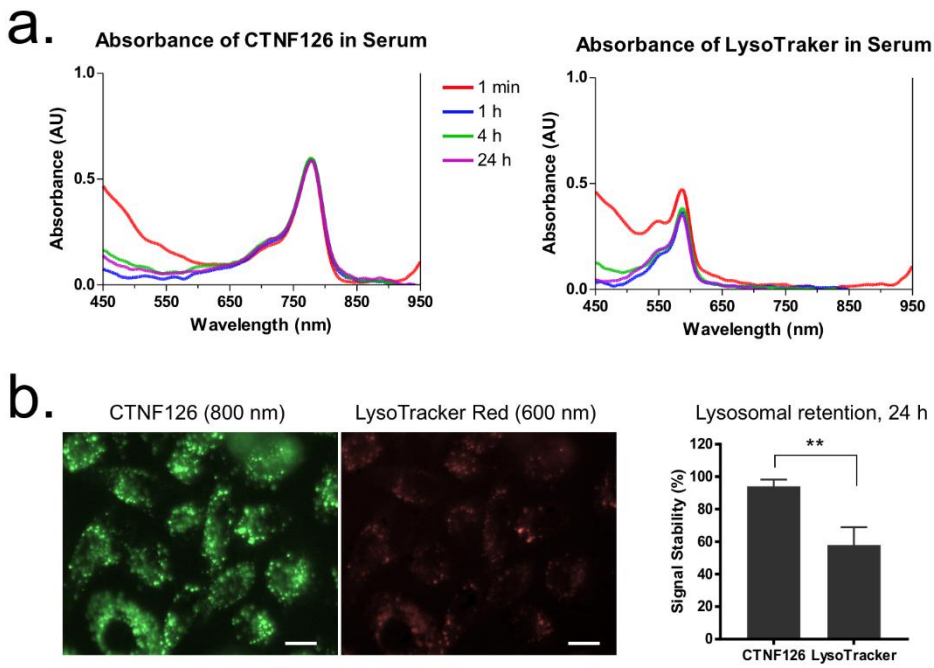

Figure 2.13 Biological stability of CTNF126 and LysoTracker. (a) Serum stability of CTNF126 (left) and LysoTracker (right) was measured in growth media at 37 °C for 1 – 24 h post-incubation. (b) Lysosomal retention of CTNF126 (left) vs. LysoTracker (right) in PC3 cells at 24 h post-incubation (n = 5, mean ± s.d., **P <0.01). Scale bar = 10 μm.

2.4 Summary

In this study, a novel NIR bioprobe CTNF126 was synthesized with excellent optical properties (i.e., high extinction coefficient, quantum yield, and photostability) for the purpose of sequential cell tracking from the body to microscopy. CTNF126 can withstand all thermal and chemical steps in histological tissue processing while retaining stable NIR fluorescence. We proved that CTNF126 is lysosome fixable with outstanding physicochemical and optical properties in serum containing media as well as organic solvents, enabling tracing of single cells for determining the mechanism of various diseases in the body. The lipophilic cation structure allows cellular membrane permeation, and the primary amine is used for rapid sequestration followed by efficient intracellular fixation by formalin through reductive amination. This ionizable amine group also reduces the risk of efflux of NIR fluorophores from the cells. Therefore, CTNF126 will be useful in staining various types of living organisms to gain direct evidence of their *in vivo* and *ex vivo* fate at the single cell level.

CHAPTER THREE: DUAL-CHANNEL FLUORESCENCE IMAGING OF HYDROGEL DEGRADATION AND TISSUE REGENERATION IN THE BRAIN

3.1 Introduction

Brain diseases and traumatic injuries such as strokes are often incurable due to the lack of adequate medical treatment, leaving permanent tissue damage that often result in neurological disabilities [61, 62]. It was recently discovered that the brain has neurogenic progenitor cells (NPC), and its capacity for vasculature and tissue de novo formation can be promoted by providing an artificial extracellular matrix for cell infiltration and differentiation [63, 64]. Various compositions of biomaterials have therefore been investigated, including modified hydrogels, that showed promising potential for the repair of brain tissue [65, 66]. Although the therapeutic feasibility of injectable hydrogels for the treatment of brain tissue damage and stroke cavity is generally accepted, their *in vivo* behavior and contribution to brain tissue regeneration remains poorly understood [18, 37, 67].

The major challenge with neural damage treatments that utilize scaffolds is the lack of availability of tissue-specific contrast agents and *in vivo* imaging system that can provide accurate information on the efficacy and behavior of injected hydrogel on tissue ingrowth [37, 68]. A

combination of fluorophore-labeled scaffold and Magnetic Resonance Imaging (MRI) has been used to achieve multimodal image analysis; however, MRI images only suggest the onset of vascularization within the scaffold [33, 34]. Spatial overlap between fluorescence and MRI images cannot be attained to provide precise information on tissue regeneration. The current standard method used to show scaffold response to tissue growth is the *ex vivo* histological analysis of immunohistochemistry against specific antigens at the microscopic level [69, 70]. Thus, it is difficult to evaluate the overall interaction/integration with the host tissue/cells and the implanted hydrogel in a continually changing *in vivo* environment.

We hypothesized that multispectral near-infrared (NIR) fluorescence imaging could provide simultaneously monitoring of cell/tissue infiltration (NIR #1) and scaffold degradation for the optimization of the composition of scaffold (NIR #2), leading to efficient treatment outcomes. In this study, we have fabricated hydrogels composed of hyaluronic acid (HA) and gelatin to mimic the mechanical properties of native brain tissue by providing extracellular matrix support, with improved cell infiltration and proliferation. Dual-channel fluorescence imaging was performed to test the efficacy of the hydrogels by utilizing NIR brain-specific contrast agents and conjugating fluorophore to the hydrogels in 700 and 800 nm channels, respectively. In addition, we

applied image segmentation analysis to the therapeutic region of the brain to provide precise visual information as well as quantitative data on the tissue ingrowth over the regeneration period.

3.2 Materials and methods

3.2.1 NIR fluorophores and hydrogels

Type A gelatin (40 - 50 kDa) from porcine skin, Oxazine1 (Ox1), and tyramine hydrochloride were purchased from Sigma-Aldrich (St. Louis, MO), and hyaluronic acid (40 - 60 kDa) were from Lifecore Biomedical (Chaska, MN). ZW800-3a was synthesized as previously reported and used for conjugation with the gelatin via the EDC/NHS coupling chemistry [47]. Briefly, 7.86 mg of ZW800-3a was added to 1 mL of distilled water containing 9.585 mg of EDC, and 10.85 mg of sulfo-NHS and shaken at room temperature for 30 min. Gelatin (1 wt%) was dissolved in 20 mL of distilled water at 60 ° C and pH was adjusted to 8.5 by adding NaOH. After gelatin has completely dissolved, pre-activated ZW800-3a NHS ester was slowly added and then the mixture was shaken for 1 h. Unconjugated dyes were filtered using dialysis and the final product was lyophilized. To prepare hyaluronic acid-tyramine conjugate (HA-ty), 1.437 g of EDC, 0.863 g of NHS and 1.302 g of tyramine were added to 1.0 g of HA sodium salt dissolved in 100 mL of

distilled water. Unconjugated tyramine was filtered using dialysis and HA-ty was collected after lyophilization. The final product was analyzed by NMR and UV spectroscopy and 33% of degree tyramine substitution was confirmed.

3.2.2 Optical property measurements

Absorbance and fluorescence were measured using fiber optic HR2000 (200-1100 nm) spectrometers by a 5 mW, 655 nm laser diode (Opcom Inc, Xiamem, China) coupled through a 300 mm core diameter. NA 0.22 fiber (Fiberguide Industries, Stirling, NJ). 5 x 10^{-6} M of each fluorophore solution was prepared in 10% fetal bovine serum (FBS) in PBS. In silico calculations of physiochemical properties such as molecular weight, charge distribution, logD at pH 7.4, pKa, rotatable bonds were calculated using JChem calculator plugins (ChemAxon, Budapest, Hungary). Data was plotted using Prism7 software (GraphPad, San Diego, CA) and Microsoft Excel (Redmond, WA).

3.2.3 Analysis of mechanical properties

The Young's modulus of hydrogel was evaluated by Ultimate Testing Machine (UTM, 100N of the load cell, EZ-SX STD, Shimadzu, Japan). Briefly, the hydrogel was crosslinked overnight

into customized PDMS mold (diameter: 8 mm, thickness: 2 mm). Then, the samples were loaded on the holder and performed the test with 0.5 mm/min of the probe speed. The Young's modulus was calculated in the range of strain from 5% to 15%. All the experiments were triplicate.

3.2.4 Rheological analysis

The viscoelastic properties of hydrogel were evaluated in Anton Paar Demo Lab using rheometer (MCR 302, Measuring cell: P-PTD & H-PTD 200, Measuring System: pp25, Anton-Paar, Austria). All the samples were prepared in PDMS mold (diameter: 8 mm, thickness: 2 mm). At first, we conducted frequency sweep. Briefly, the sample was loaded on the plate, and detection probe was positioned on the sample with 2 mm gap. The G' and G" was measured according to variation of frequency from 1 to 100 Hz. In frequency sweep, the strain was fixed at 1%. To evaluate a critical strain, we checked the viscoelastic properties with increasing strain from 0.1 to 500%.

3.2.5 Live cell labeling and tracking in the NIR hydrogel

C2C12, mouse myoblast cells, was cultured with DMEM/F12, supplemented with 10% FBS and 1% P/S and incubated at 37 °C in a

humidified 5% CO_2 incubator. When cells reached 80-90% confluence, the seeded cells were rinsed twice with PBS and ESNF13 (cell tracking NIR fluorophore) was added at a concentration of 5 μM and incubated for 20 min at 37 °C. Cells were washed three times with PBS and detached with trypsin and centrifuged and the supernatant was removed. These cells were then embedded in the mixture of 1wt% HA and 1 or 3wt% NIR-gel and SA_ty was added to five a final density of 4 x 10^5 cells/mL and then 100 μL was transferred to a 24-well plate. After 30 min incubation in 37 °C, culture media was added to provide nutrients to the cells. The cells and hydrogel were observed for 12-d under the 4-channel TE2000 NIR fluorescence microscope. Two custom filter (Chroma Technology Corporation, Brattleboro, VT) composed of 650 ± 22 nm and 750 ± 25 nm excitation filter, 675 nm and 785 nm dichroic mirrors, and 710 ± 25 nm and 810 ± 20 nm emission filters were used to detect cells and NIR hydrogel, respectively. Fluorescent intensity (FI) of region of interest (ROI) was quantified using image J software (NIH, Bethesda, MD). Results were presented as mean ± standard deviation (s.d.).

3.2.6 *In vitro* cell viability test

The number of viable cells was counted at each time point by

separating the fluorescence (FL) signal of the cells from the background. To separate the FL signal of cells, we first converted the images to binary format using Image J software (NIH, Bethesda, MD). The total FL area was then calculated and divided by the average area of single cell to determine the number of cells. The proliferated cells were quantified by comparing the number of mother cells and daughter cells using Image J software.

3.2.7 Animal models for hydrogel implantation

All animal studies were performed under the supervision of MGH IACUC and housed in an AAALAC certified facility with approved protocol #2016N000622. C57BL/6 mice (8 weeks) and NCRNU nude mice (20–30 g, 6–8 weeks) were purchased from Jackson Laboratory and Taconic Farms, respectively. Mice were anesthetized with an intraperitoneal injection of ketamine (100 mg/kg) and xylazine (10 mg/kg). Nude mice were used for subcutaneous implantation of the NIR hydrogel. 100 μL of NIR hydrogel were injected into each side of the flank (n = 3). Noninvasive optical imaging was performed from the same animal every week for 3 weeks using the K-FLARE imaging system.

3.2.8 Optical fluorescence imaging system and quantification

For dual-NIR channel imaging, 1 mW/cm2 of a 660-nm excitation light (NIR #1) and 3.6 mW/cm2 of a 760-nm excitation light (NIR #2) were used with white light (400-650 nm) at 5,500 lux. Simultaneous color images (512 × 512 pixels) with the choice of either 700 nm or 800 nm fluorescence images were acquired using an AD-130GE camera (JAI, Yokohama, Japan) installed with custom dual bandpass prism (channel 1: 710/50, channel 2: 780lp). The imaging system was remotely controlled by custom software at rates up to 15 Hz, except for field of view that was manually adjusted by a 3CCD zoom lens (Goyo Optical Inc., Saitama, Japan). In the color-NIR merged image, 700-nm fluorescence and 800-nm fluorescence were pseudo-colored red and green, respectively. The imaging head was positioned at a distance of 9 in from the surgical field, and all NIR fluorescence images have identical exposure times and normalizations.

3.2.9 Intracranial transplantation of NIR hydrogel and brain tissue imaging

C57BL/6 mice were used for intracranial transplantation. 20 μL of NIR hydrogel was injected using a 28-gaugue needle with the following coordinates: anterior-posterior = 1 mm, medial-lateral =

2 mm, and dorsal−ventral = 2.5 mm. Animals were injected with 100 nmol of Ox1 intravenously 1 h prior to imaging on each day (1−, 7−, 14−, and 28−d post−transplantation). After intraoperative imaging, animals were sacrificed, and each brain was extracted for dual−channel imaging. Whole brain images were taken first, and then the brain was cut consecutively with a 2 mm thickness in coronal sections. Hydrogel−injected brain sections were imaged simultaneously at 700 nm (NIR #1) and 800 nm (NIR #2) channels at various exposure times.

3.2.10 Histological analysis and NIR fluorescence microscopy

NIR hydrogel−injected brain samples were mounted in Tissue−Teck OCT compound (Fisher Scientific, Pittsburgh, PA) and flash−frozen in liquid nitrogen. These samples were cut to a 10 μm thickness and stained with hematoxylin and eosin (H&E) and fluorescence microscopy was performed to acquire images. NIR fluorescence microscopy was performed on TE2000 described above.

3.3 Results and Discussion

3.3.1 Engineering of injectable NIR hydrogels

NIR fluorescence has many advantages for biomedical imaging, including relatively low tissue absorption, reduced scattering, and minimal autofluorescence [20, 71, 72]. We developed injectable NIR hydrogels by conjugating an 800 nm indocyanine NIR fluorophore ZW800-3a through the carboxylic functional group, which enables conjugation with an amine group in gelatin (Fig 3.1). To avoid any adverse effects, it is crucial for the engineered hydrogel to have minimum *in vivo* protein interactions after degradation. ZW800-3a has been reported to have a low level of toxicity and fast excretion because of its charge distribution and hydrophilicity (logD at pH 7.4 = −1.63) [47, 48]. The physiochemical and optical properties of ZW800-3a can be found in Fig 3.2-3.3.

Hydrogels composed of hyaluronic acid (HA), major components within brain ECM, and gelatin are known to provide an extracellular matrix for neural differentiation [73]. Therefore, we initially prepared tyramine-conjugated HA (HA-ty) and crosslinked with NIR-gelatin using recombinant tyrosinase isolated from Streptomyces avermitilis (SA_Ty) [74]. Our previous study has demonstrated that the SA_Ty allow ultra-fast conversion of monophenol to crosslinkable o-quinone groups in both tyramine

conjugated HA and gelatin [75]. This allow tyrosinase-dependent crosslinkable and adhesive hydrogels to be formed from HA-ty. Furthermore, addition of NIR-gelatin in HA-ty allows formation of stiffer and cell-adhesive NIR hydrogel crosslinking of HA-ty and gelatin.

The schematic overview of the dual-channel monitoring of tissue growth and hydrogel behavior is shown in Figure 3.1b. The multispectral FLARE imaging system provided simultaneous acquisition of color video and two independent channels of NIR fluorescence in the range of 650-900 nm (Fig 3.4). We utilized the 800 nm channel to track NIR hydrogel behavior on 1-, 7-, 14-, and 21-d post-transplantation and the 700 nm channel for monitoring brain tissue ingrowth by the intravenous administration of Ox1 1 h prior to performing dual-channel fluorescence imaging. Oxazine derivatives with low molecular weight (<500 Da) and medium lipophilicity (logD 1-3) can cross intact blood-brain-barrier (BBB) and accumulates in the parenchyma of the brain [76]. We discovered that Ox1, phenoxazine structure fluorophore emitting at 700 nm, has significant uptake into the brain for detection after intravenous administration. The physiochemical and optical properties of Ox1 can be found in Fig 3.2-3.3.

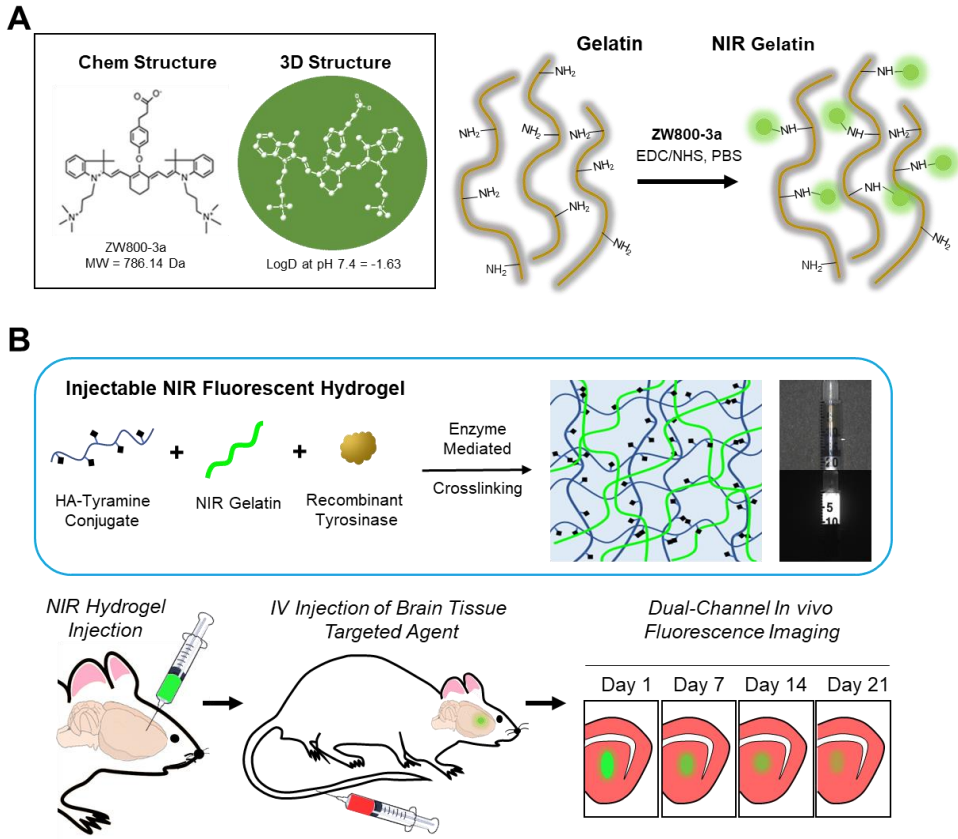

Figure 3.1 Dual-channel imaging of NIR hydrogel and brain tissue ingrowth. (A) Chemical structure of ZW800-3a and its chemical conjugation on gelatin. (B) Overall Strategy of multichannel NIR imaging for the *in vivo* assessment of tissue ingrowth and scaffold degradation. Preparation of injectable NIR hydrogel by crosslinking tyramine conjugated hyaluronic acid (HA) and NIR-gelatin with tyrosinase for the intracranial injection. Intravenous administration of Ox1 1 h prior to *in vivo* imaging of the brain. Dual-channel imaging of tissue ingrowth and hydrogel degradation under 700 nm (red color) and 800 nm channel (green color), respectively. Scale bar = 5 mm.

A

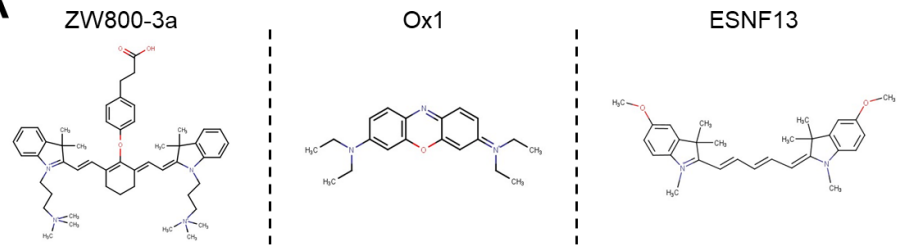

B

Physiochemical & Optical Properties	ZW800-3a	Ox1	ESNF13
MW	786.14	324.45	443.61
Em / Ex	774 / 790	655 / 670	674 / 700
Charges (+/-)	+3 / - 1	+1 / 0	+1 / 0
Log*D*, pH 7.4	-1.63	0.33	3.24
Acidic / Basic p*K*a	4.40 / 1.69	N/A / 3.91	N/A / 2.57
Rotatable Bonds	16	5	5
H-Bond Acceptor / Donor	4 / 1	3 / 0	3 / 0
Polar Surface Area	52.78	27.84	24.71
Extinction Coefficient ($M^{-1}cm^{-1}$)	309,000	123,000	117,000
Quantum Yield (%)	16.1	14.0	4.9

Figure 3.2. Physiochemical & optical properties of ZW800-3a, Ox1, and ESNF13. Physicochemical properties were calculated using JChem calculator plugins (ChemAxon, Budapest, Hungary). Optical properties were measured in FBS supplemented with 50 mM HEPES, pH 7.4 at a concentration of 1-5 μM. For QY measurements, Oxazine 725 in ethylene glycol (QY = 19%) and ICG (QY = 13%) in DMSO were used as calibration standards under conditions of matched absorbance at 660 nm (Ox1 & ESNF13) or 770 nm (ZW800-3a), respectively.

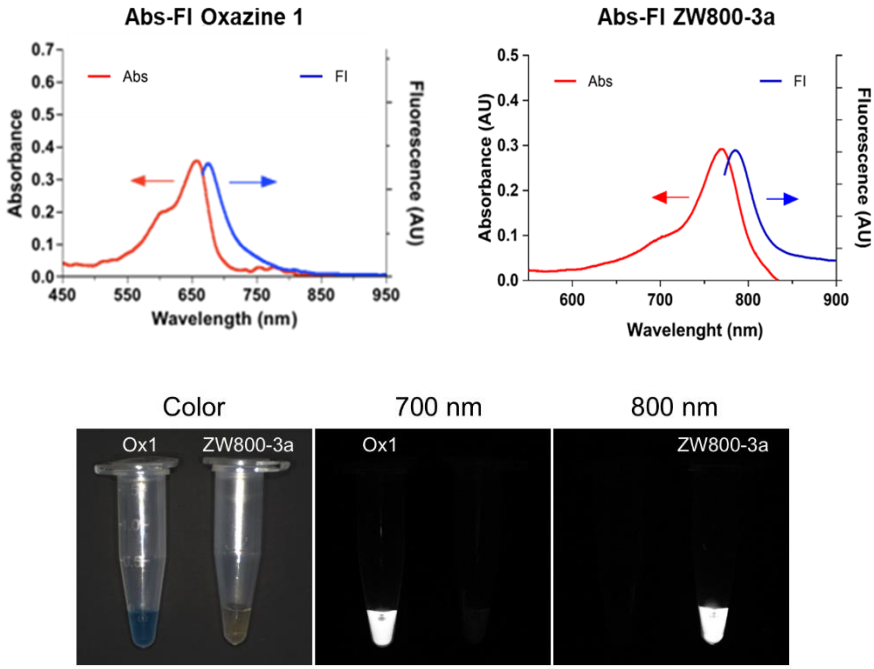

Figure 3.3 Optical properties of Ox1 and ZW800-3a. Absorbance and fluorescence emission spectra of each fluorophore in 10% BSA (bovine serum albumin) in PBS (5 μM) (top). Dual-channel fluorescence images of Ox1 and ZW800-3a acquired in 700 and 800 nm channels of the K-FLARE imaging system (bottom).

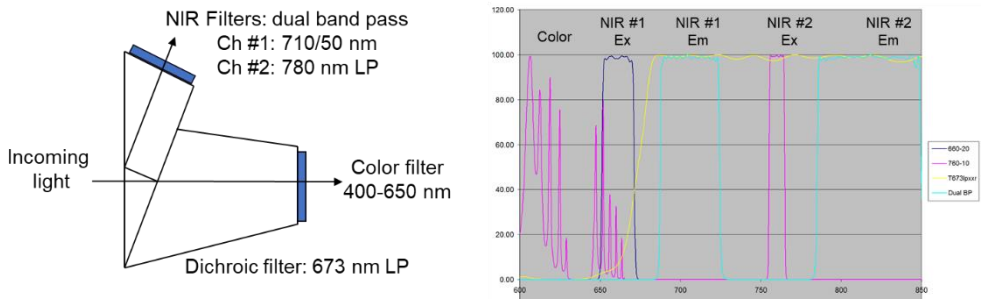

Figure 3.4. Optical light path and filtration for the K-FLARE imaging system. A color camera, and two intendent and simultaneous NIR camera (700 nm emission and 800 nm emission) are built in the head of the system (left). Filter profile for the color and NIR channels (right).

3.3.2 Mechanical and rheological property of NIR hydrogels

Mechanical and rheological characterization of the injectable NIR hydrogel is essential to achieve optimal therapeutic efficacy, as they play critical role on the migration, proliferation, and differentiation of neural stem cells. The stiffness of hydrogel provides the structural support within the damaged brain cavity while influencing cell invasion and phenotype of neural progenitors populations [77]. In addition, the retention of scaffold within the brain cavity and the associated host response is highly dependent on the compatibility with the implanted substrate; therefore, it should have brain-tissue-like characteristics [78].

Two different NIR hydrogels with different compositions, 1% and 3% of NIR-gelatin with fixed concentration of 1% HA, was prepared, and young's modulus (Y) was measured (Fig 3.5a). Young's modulus of 1% NIR-gelatin ranged between 3.9 to 7.3 kPa and 3% NIR-gelatin ranged between 31.2 and 49.7. We have compared the modulus of brain tissue from other studies and the reported range was between 3 and 10 kPa [79-81]. Interestingly, numerous studies have shown that neural stem/progenitor cell proliferation and differentiation exhibited maximal potential on the soft surfaces (Y = ~ 3.5 kPa) [77], highlighted red in the graph. Areas with higher nuclear density within the brain were also

reported to be softer when compared with the lower nuclear density area [82]. 1% NIR hydrogel has a better mechanical match with the brain tissue as it mimics the soft mechanical environment for neural stem cell differentiation.

Rheological property of the hydrogel is important because when injected into the defect cavity of the brain, the implant should have enough viscoelasticity to be able to hold the original injected form and provide the matrix for the neural cells. The amplitude sweep test of the 1% and 3% NIR-gelatin was performed at a constant frequency of 1% to evaluate the rheological properties of the hydrogels (Fig 3.5b). The crossover of G' and G" for 1% and 3% NIR-gelatin was at about 80% and 150% strain, respectively. The internal structure of hydrogel broke at the crossover point of G' and G"; beyond this point, the original structure of the NIR hydrogel was lost. Next, we measured frequency sweep to determine the dynamic behavior of the NIR hydrogel (Fig 3.5c). Compared with 1% and 3% composition of NIR-gelatin, 3% had higher storage (G') and loss (G") than 1% NIR-gelatin, indicating 1% NIR-gelatin is less stiff than 3% NIR-gelatin. Both 1% and 3% NIR-gelatin had high critical strain and elasticity and can withstand relatively large deformation force while only 1% NIR-gelatin exhibits the softness essential for neurogenesis.

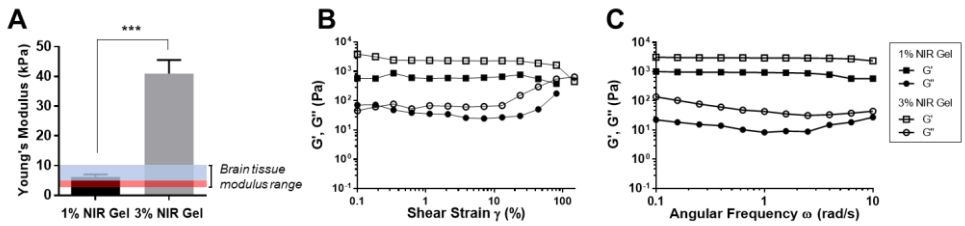

Figure 3.5 Mechanical and rheological evaluation of NIR hydrogel. (A) Young's Modulus of NIR hydrogel of different compositions. The highlighted blue and red region indicates range of young's modulus of brain tissue. The highlighted red region is a range of high neural proliferation and differentiation. (B) Amplitude sweep of NIR hydrogels. (C) Frequency sweep of NIR hydrogels. Data are representative of n=3 samples.

3.3.3 *In vitro* cell viability test of NIR hydrogels

Next, we investigated *in vitro* cell viability and proliferation of C2C12 in 1% and 3% NIR-gelatin encapsulated system. C2C12 was labeled with 700 nm NIR fluorophore, ESNF13, previously reported for the use of the longitudinal cell tracking with an excellent optical property [34]. The molecular structure and optical properties of ESNF13 can be found in Fig 3.2. After 30 min incubation with 5 μM of ESNF13, C2C12 were detached from the Petri dish and embedded in 1 wt% or 3 wt% NIR-gelatin with a fixed concentration of HA-ty (1 wt%). Tyrosinase (SA_ty) (5 U) was added to initiate hydrogel crosslinking, and the cell-laden hydrogel mixture was immediately transferred to 24 well plates. Culture media was added to provide the nutrient for the cells and live cell imaging was performed using an NIR fluorescence microscope for up to 2 weeks. The number of viable cells was counted at each time point based on the fluorescence signal of the cells in the 700 nm channel (Fig 3.6). The total area of the cells was calculated based on the FL signal and divided by the area of a single cell to determine the number of proliferated cells at each time point. Cells embedded in 1% NIR-gelatin had steady proliferation rate (Fig 3.7); however, cells embedded in 3% NIR-gelatin stopped proliferating 3-d post-incubation, and most of the cells were dead and the

fluorophores inside the cells eluted to the nearby hydrogel by 8-d post-incubation (Fig 3.8). Next, we quantified and plotted signal intensity changes in both the cells and NIR hydrogel in 700 and 800 nm channels, respectively (Fig 3.6b). We observed a gradual intensity decrease of the cells over time, as an indication of active proliferation in 1% NIR-gelatin. When the cells proliferate, the number of fluorophores that are uptaken gets divided between the mother and daughter cells. We also saw a gradual decrease in the intensity of NIR hydrogel as it degraded.

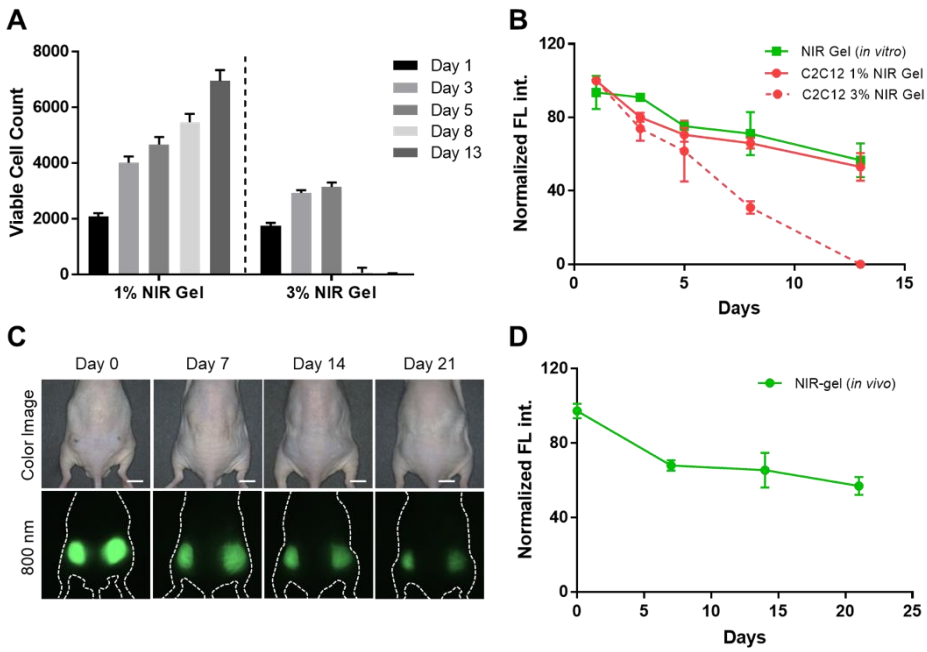

Figure 3.6 *In vitro* and *in vivo* viability and stability test. (A) Viability of myoblasts (C2C12) in 1 and 3 wt% of NIR-gelatin with fixed amount of HA-ty (1 wt%) for up to 2 weeks. (B) *In vitro* quantification of signal change of C2C12 labeled with ESNF13 (5 μM) and NIR hydrogel over the time course. NIR hydrogels in 10% FBS were used as control. (C) Real-time longitudinal noninvasive imaging of NIR hydrogel (100 μL) injected into the subcutaneous of nude mice for up to 3 weeks. (D) Quantitative plotting of the *in vivo* signal reduction of NIR hydrogel over time. Scale bars = 1 cm. Data are representative of n = 3 samples or animals.

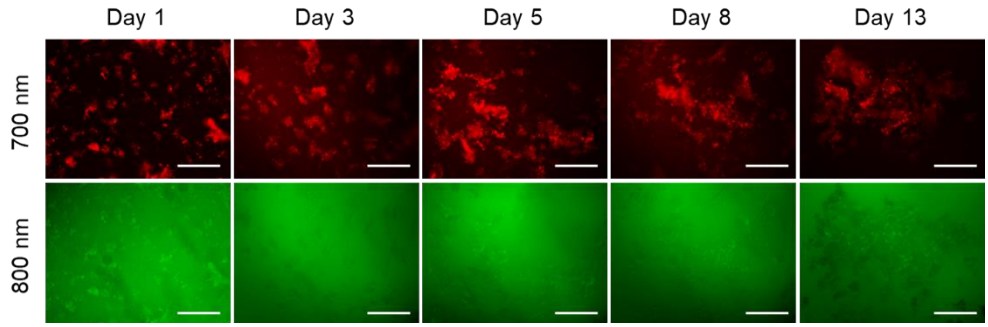

Figure 3.7 Live cell imaging of C2C12 embedded in the NIR hydrogel. C2C12 (700 nm) stained with ESNF13 (5 μM) were embedded in 1% NIR hydrogel (800 nm) and observed for up to 2 weeks. All images were taken at identical exposure and normalized. Scale bars = 100 μm.

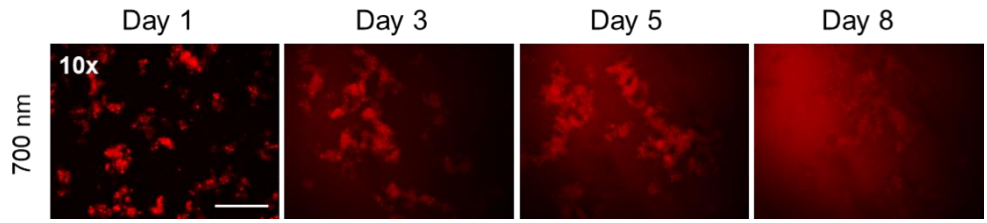

Figure 3.8 Live cell imaging of C2C12 embedded in 3% NIR hydrogel. C2C12 (700 nm) stained with ESNF13 (5 μM) were embedded in 3% NIR hydrogel and observed for up to 8 days. All images were taken at identical exposure and normalized. Scale bar = 100 μm.

3.3.4 *In vivo* physiological stability and degradation of NIR hydrogels

To investigate the optical- and bio-stability of ZW800-3a after its conjugation with the hydrogel, we performed a real-time non-invasive longitudinal monitoring of the hydrogel in nude mice for up to 3 weeks. NIR hydrogel (100 μL) was injected into subcutaneous of the flank region of nude mice and NIR signal was quantified and plotted every 3-5 d. (Fig 3.6c-d). Shrinkage of the hydrogel was observed after initial swelling. Previously, different groups have attempted to label hydrogel with commercially available fluorophores (e.g., Alexa488) that have lower excitation and emission wavelength [83]. These fluorophores are not stable enough to track the hydrogel for an extended period of time. In addition, we believe covalent conjugation of the fluorophore prevented staining nearby tissue, minimizing false margin of the implanted hydrogel. We confirmed this by removing the skin and observed the fluorescence signal only in the hydrogel (Fig 3.9a). The composition of NIR hydrogel is degradable by endogenous hyaluronidase. We consequently traced degraded hydrogel on 21-d post-injection, and most of them were found in the intestine, suggesting hepatobiliary clearance of disassembled hydrogel (Fig 3.9b).

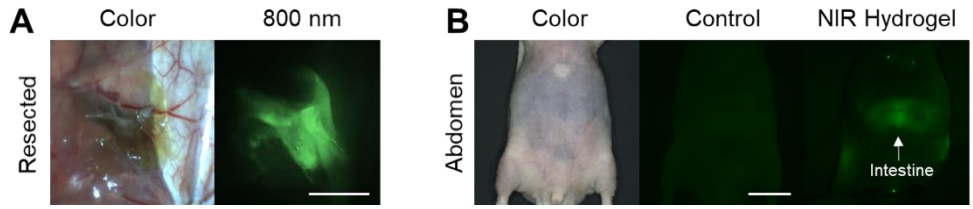

Figure 3.9 Biodistribution and clearance of NIR hydrogel. Long-term degradation and biodistribution of NIR hydrogel were imaged at 21 days post-implantation, compared with a control animal without scaffold implantation. Animals were fed white chow without chlorophyll to avoid autofluorescence. Scale bars = 1 cm.

3.3.5 Multichannel imaging of hydrogel degradation and tissue growth

Dual-channel fluorescence imaging strategy is used to track host tissue growth and scaffold degradation after brain implantation. Twenty microliters of NIR hydrogel was intracranially injected into the brain of animals by the defined coordinates on stereotactic. Ox1 (100 nmol) was intravenously administered into the same animals an hour before NIR imaging time points. Images of the whole and sectioned brain tissues were acquired in 700 nm (red) and 800 nm (green) channels simultaneously, followed by merging into colocalize ingrowth area over the implanted scaffold (Fig 3.10). We also performed *in vivo* dual-channel imaging to show fluorescence signal of the NIR hydrogel transplanted brain through the intact skull and after skull removal 7-d post-implantation (Fig 3.11).

After brain damage, limited blood supply due to the damaged vasculature with increases inflammatory and immune response prevents the delivery Ox1 to the damaged area [84]. We observed high scaffold signal on 1-d and 7-d post-implantation and no significant signs of tissue growth within the hydrogel, whereas substantial decreased signal was observed in the scaffold on 14-d post-implantation. In the merged images, the area where tissue increased tissue growth has mixture of red and green color

resulting light green to orange.

In addition, we imaged the whole brain to diagnose any abnormal signs of intracerebral pressure build up or prevention of normal vasculature blood flow in the consequence of injecting high volume of hydrogels. We observed limited blood supply from the circulation 1-d post-injection of the hydrogel of the transplanted side of the whole brain (Fig 3.12a). Interestingly, the full blood flow to the brain was recover by 7-d post-implantation. The quick recovery of blood flow in the brain suggests the NIR hydrogel did not cause vasculature damage to the host tissue as the formulation of the hydrogel allow minimal invasiveness for the delivery and fast situ gelation prevented the large diffusion of the biomaterial into parenchyma. We also observed migration of degraded hydrogels in all directions to the nearby tissue in the 800 nm single channel with increased distance from the injection site with prolonged implantation period (Fig 3.12b). The advantages of using optical imaging is high sensitivity and spatial resolution, which have the ability to obtain structure and physiological information. From the acquired images, we developed a quantification method to accurately calculate the percentage of ingrown tissue within the hydrogel.

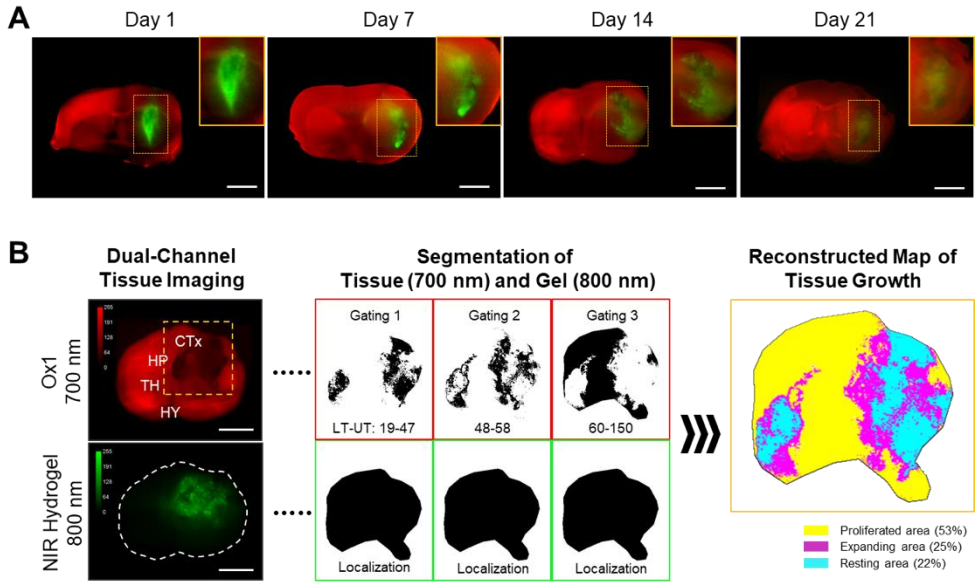

Figure 3.10 Dual-channel imaging of brain tissue growth and NIR hydrogel. (A) NIR hydrogel (20 μL) was injected into the brain of animals and Ox1 (100 nmol) was administered to the same animal an hour prior to the dual-channel imaging. Brain tissue ingrowth (red) and NIR hydrogel (green) degradation observed in the merged image. Sample thickness = 2 mm. (B) Spatial segmentation analysis of the NIR image for the quantification and visualized dynamic color mapping of the tissue ingrowth. Scale bars = 2.5 mm.

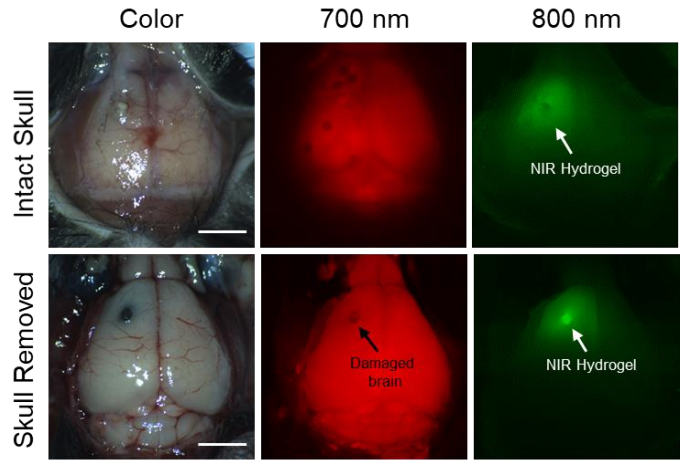

Figure 3.11 Dual-channel *in vivo* imaging of brain tissue growth and NIR hydrogel. NIR hydrogel (20 μL) was injected into the brain of animals and Ox1 (100 nmol) was administered to the same animal an hour prior to the dual-channel intraoperative imaging at day 7-d of post-implantation. Brain tissue (red) and NIR hydrogel (green) degradation observed with intact skull and after removing the skull. Scale bars = 2.5 mm.

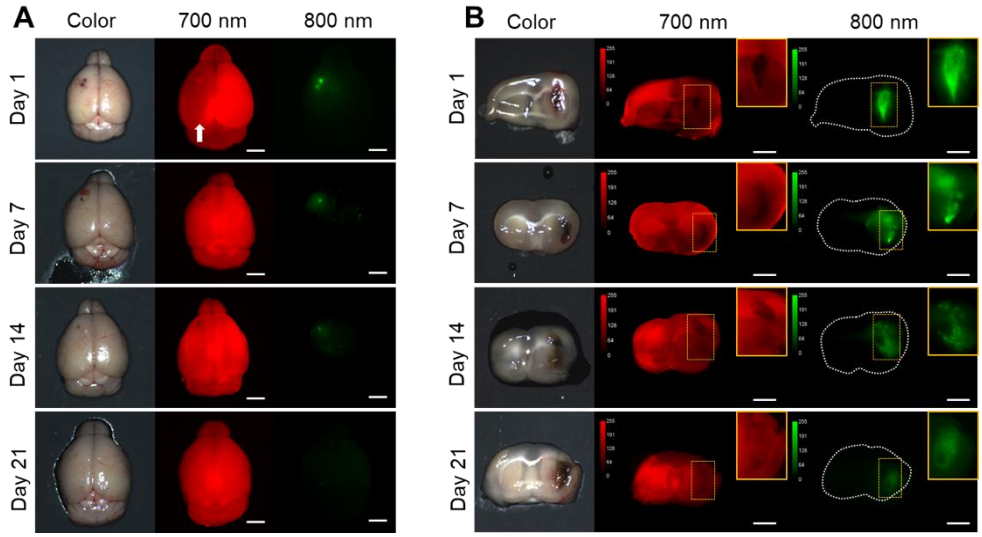

Figure 3.12 Dual-channel simultaneous imaging in the brain. (A) Whole brain imaging of the of Ox1 (700 nm) and NIR hydrogel (800 nm) distribution change over time. (B) Intraoperative NIR imaging of tissue ingrowth and NIR hydrogel at 700 and 800 nm channel, respectively. Sample thickness = 2 mm. Scale bars = 2.5 mm.

3.3.6 Quantitative annotation of brain tissue ingrowth

Image segmentation is used in the medical field to provide precise analytical information. It utilizes segmentation by labeling every pixel in an image where similar characteristics are assigned with the same label. We applied this method to quantify and annotate the regenerated tissue based on the FL intensity in the therapeutic region where hydrogel has been implanted (Fig 3.13a). Three segmented binary images were generated by setting the lower and upper threshold value based on the histogram intensity of Ox1 (700 nm) at each time point. These binary images were then color-coded, merged, and reconstructed to provide dynamic color mapping to show clear boundaries within the therapeutic area. For quantitative analysis, the number of pixels in each color were calculated to determine the overall percentage of proliferation (yellow), active expansion (magenta), and the resting (cyan) area (Fig 3.13). With our multispectral imaging system and quantification method, we can localize the damaged area with limited tissue growth (resting area) after the initial treatment and can be used provide a next treatment plan.

3.3.7 Histological analysis using NIR fluorescence microscopy

Tissue ingrowth and scaffold degradation were evaluated at a

microscopic level by collecting brain samples after the dual-channel imaging. Hematoxylin and eosin (H&E) staining was performed on the samples cut at 10 μm and observed through NIR fluorescence microscope (Fig 3.13b). The microporous structure of hydrogel was observed 1-d post-implantation and was well maintained up to 21-d in the degradation process. We found a reduction in the fluorescence signal intensity and the decrease in the thickness of hydrogel after the initial swelling. Cell infiltration and adhesion around the hydrogel were observed 7-d post-implantation, indicating rapid cellular infiltrations without the need for bulk degradation. The cells continue to infiltrate and proliferate within the hydrogel, expanding the ingrowth area by 14-d and even more on 21-d post-implantation. These histological evaluations were consistent with *in vivo* fluorescence images. Therefore, a combination of *in vivo* imaging and histological analysis can provide substantial information needed to determine the regeneration capacity of the implanted scaffold. Alternatively, this technique can be combined with fluorescence protein expressing cells to monitor *in vivo* behavior of transplanted cells within the hydrogel.

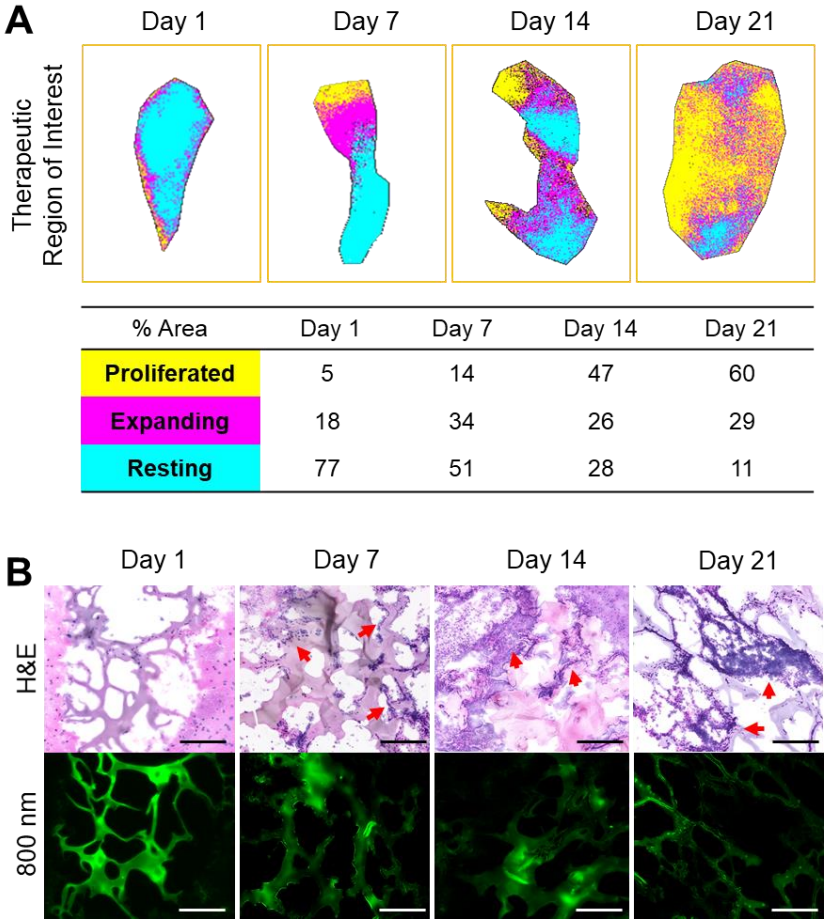

% Area	Day 1	Day 7	Day 14	Day 21
Proliferated	5	14	47	60
Expanding	18	34	26	29
Resting	77	51	28	11

Figure 3.13 Reconstructed map of tissue ingrowth and histological analysis at each time point. (A) Time course *in vivo* localization and quantification of brain tissue growth within the therapeutic region of implanted hydrogel. (B) H&E and NIR imaging of scaffold from the brain samples collected at 1−, 7−, 14−, and 21−d post−implantation of the hydrogel. Sample thickness = 10 μm. Scale bars = 50 μm.

3.4 Summary

In this study, we have developed a novel dual-channel optical imaging technique to simultaneously track scaffold degradation and brain tissue ingrowth over the complete regeneration period. High-resolution imaging with multispectral capability will be further useful to localize and quantify brain tissue growth and to monitor the therapeutic efficacy of scaffold in the brain. NIR-II imaging window will be absolutely beneficial for this application, and we believe that our multispectral optical imaging technique could play a significant role in translating regenerative medicine to the clinic with an aim to provide a high quality of life to patients and their families after recovering from devastating brain diseases.

CHAPTER FOUR: CONCLUDING REMARKS

4.1 Summary

Optical fluorescence imaging has made significant insights for clinical usage by allowing non-invasive visualization of cellular and molecular processes in living subjects [85]. Thus it aids in tracking the progress of delivered cells, checks viability, and overall monitors the cells during cell based therapy [86]. Nonetheless, no single modality is currently impeccable in every aspect to meticulously monitor cell-based therapy. As it is important to analyze the efficacy of transplanted cells, extensive investigations will hopefully further evaluate the optical imaging of the cell's fate and its functional therapeutic effects. Developing probes that can best provide sensitivity to track the viability of transplanted effector cells is important as well as for multimodal imaging of optical imaging with other techniques like fluorescence lifetime imaging and photoacoustic imaging. Cell-based therapy has great potential to provide a new level of treatment and non-invasive sequential imaging is essential for successful clinical therapy.

4.2 Future perspective

Optical imaging and NIR probes designed for cell-based therapy has made significant contributions and will continue to provide important insights. However, optical imaging itself has limitations, such as in-depth resolution and difficulties in quantification. Therefore, development of multimodal probes for both optical and radioisotopic or magnetic imaging to overcome pros and cons of each imaging method can advance the therapy for future clinical use. Also, noninvasive imaging modalities, such as fluorescence lifetime imaging and ultrasound elasticity imaging (UEI) have been developed to monitor degradation of implanted scaffold and tissue ingrowth [87].

4.2.1 Multimodal Imaging

When an optical imaging modality is used in combination with other modalities of imaging, this becomes multimodal imaging. The approach of this modality can be by either obtaining the images asynchronously (at different times) or synchronously (at the same times) [88]. When acquired asynchronously the images are fused through digital image manipulation and the modality is limited because the images are gained in different times using separate machines at possibly different positions. The synchronous imaging,

therefore, is considered a better option with the consistency in time and space.

For dual modal tracking of transplanted mesenchymal stem cells (MSCs) after myocardial infarction, magnetic resonance imaging (MRI) and NIR optical imaging were utilized. These two were chosen to explore the effects of different delivery modes of MSCs on cell retention time and cardiac function determined by measuring the iron and optical signals in explanted organs. The combination of the modes enabled to conclude that IM injection of MSCs increased cell engraftment within infarcted hearts and improves cardiac function [88]. Multimodal imaging –with bioluminescence imaging (BLI), fluorescence imaging (FI) and MRI– used CyI dyes and ultra-small super-paramagnetic iron oxide (USPIO) particles as labels to trace transplanted bone mesenchymal stromal cells (BMSCs) in mouse model of acute myocardial infarction. BLI was revealed to be the optimal imaging method *in vivo*, compared to FI [89].

4.2.2 Fluorescence Lifetime Imaging

Fluorescence lifetime imaging (FLIM) generates contrast by measuring the NIR fluorophore' s time dependent intensity decay which minimizes photon scattering in thick layers of samples [3,

90]. This imaging technique modulates the fluorescence excitation light and has a more specific approach to identify the target [91].

Fluorescence lifetime imaging enables the detection of composite molecular assemblies within a single voxel for studies of cell function and communication with subcellular resolution in optically transparent tissues [92]. Cardiomyocytes and cancer cells showed contrasting uptake patterns of gold-doxorubicin through FLIM which explained the toxicity difference [93]. These results suggest that stable conjugates of nanoparticles to doxorubicin may be helpful in treating cancers while simultaneously sparing healthy tissue.

Lung stem/progenitor cells are potentially useful for regenerative therapy, for example in repairing damaged or lost lung tissue in patients. In combination with fluorescence-activated cell sorting, fluorescence lifetime imaging microscopy and immunostaining, fluorescent nanodiamonds can identify the transplanted cells *in vivo*, and track their engraftment and regenerative capabilities with single-cell resolution [94].

4.2.3 Photoacoustic Imaging

Photoacoustic imaging, which is also known as optoacoustic imaging, is an imaging modality based on the ultrasonic emission of the

absorbed energy that is converted to heat [95, 96]. This imaging modality has the potential to image human organs more efficiently in the long run with high contrast and spatial resolution as it is already being utilized clinically. Though photoacoustic imaging is limiting in the depth penetration by ultrasonic attenuation, an ultrasonic transducer is used to determine the spatial resolution. Hence, with a transducer that provides higher central frequency and broader bandwidth, higher axial resolution can be obtained.

Yang et al. showed through photoacoustic imaging that cytokine-induced killer cells labeled with gold nanorods enhanced immunotherapy efficacy by up-regulating cytokines and killed gastric cancer tissues by photothermal therapy [97].

4.2.5 NIR-II Fluorophores

Lastly, the contrast agent can only image superficial processes due to its low tissue penetration [98]. New NIR, and possibly NIR-II, contrast agents should therefore be developed to overcome these limitations. NIR-Ib and NIR-II fluorophores have an optical imaging window between 900-1,700 nm, where tissue scattering is extremely low [99]. The implementation of NIR-II fluorescence, may therefore revolutionize fluorescence imaging by improving depth penetration, spatial and temporal resolution, and SBR [100].

Until new advances are made with NIR-II imaging, the development of NIR-I contrast agents and their approval by the FDA is the rate-limiting step in the clinical utilization of intraoperative fluorescence technology.

References

[1] P.K. Nguyen, D. Nag, J.C. Wu, Methods to assess stem cell lineage, fate and function, Adv Drug Deliv Rev, 62 (2010) 1175-1186.

[2] E.A. Owens, M. Henary, G. El Fakhri, H.S. Choi, Tissue-specific near-infrared fluorescence imaging, Accounts of Chemical Research, 49 (2016) 1731-1740.

[3] S. Gioux, H.S. Choi, J.V. Frangioni, Image-guided surgery using invisible near-infrared light: fundamentals of clinical translation, Mol Imaging, 9 (2010) 237-255.

[4] E.A. Owens, S. Lee, J. Choi, M. Henary, H.S. Choi, NIR fluorescent small molecules for intraoperative imaging, Wiley Interdiscip Rev Nanomed Nanobiotechnol, 7 (2015) 828-838.

[5] H.S. Choi, Y. Ashitate, J.H. Lee, S.H. Kim, A. Matsui, N. Insin, M.G. Bawendi, M. Semmler-Behnke, J.V. Frangioni, A. Tsuda, Rapid translocation of nanoparticles from the lung airspaces to the body, Nat Biotechnol, 28 (2010) 1300-1303.

[6] J. Rao, A. Dragulescu-Andrasi, H. Yao, Fluorescence imaging in vivo: recent advances, Current opinion in biotechnology, 18 (2007) 17-25.

[7] E.A. Owens, H. Hyun, T.L. Dost, J.H. Lee, G. Park, D.H. Pham, M.H. Park, H.S. Choi, M. Henary, Near-infrared ilumination of

native tissues for image-guided surgery, J Med Chem, 59 (2016) 5311-5323.

[8] A.B. Cubitt, R. Heim, S.R. Adams, A.E. Boyd, L.A. Gross, R.Y. Tsien, Understanding, improving and using green fluorescent proteins, Trends Biochem Sci, 20 (1995) 448-455.

[9] A. Miyawaki, J. Llopis, R. Heim, J.M. McCaffery, J.A. Adams, M. Ikura, R.Y. Tsien, Fluorescent indicators for Ca2+ based on green fluorescent proteins and calmodulin, Nature, 388 (1997) 882-887.

[10] N.C. Shaner, P.A. Steinbach, R.Y. Tsien, A guide to choosing fluorescent proteins, Nat Methods, 2 (2005) 905-909.

[11] X. Shu, A. Royant, M.Z. Lin, T.A. Aguilera, V. Lev-Ram, P.A. Steinbach, R.Y. Tsien, Mammalian expression of infrared fluorescent proteins engineered from a bacterial phytochrome, Science, 324 (2009) 804-807.

[12] H.S. Choi, Nanoparticle assembly: building blocks for tumour delivery, Nat Nanotechnol, 9 (2014) 93-94.

[13] M. Longmire, P.L. Choyke, H. Kobayashi, Dendrimer-based contrast agents for molecular imaging, Curr Top Med Chem, 8 (2008) 1180-1186.

[14] M.K. So, C. Xu, A.M. Loening, S.S. Gambhir, J. Rao, Self-illuminating quantum dot conjugates for in vivo imaging, Nat Biotechnol, 24 (2006) 339-343.

[15] E.A. Owens, H. Hyun, J.G. Tawney, H.S. Choi, M. Henary, Correlating molecular character of NIR imaging agents with tissue-specific uptake, J Med Chem, 58 (2015) 4348-4356.

[16] D.S. AV, H. Lin, E.R. Henderson, K.S. Samkoe, B.W. Pogue, Review of fluorescence guided surgery systems: identification of key performance capabilities beyond indocyanine green imaging, J Biomed Opt, 21 (2016) 80901.

[17] A.W. Yang, S.U. Cho, M.Y. Jeong, H.S. Choi, NIR fluorescence imaging systems with optical packaging technology, J Microelectron Packag Soc, 21 (2014) 25-31.

[18] T. Kim, C. O'Brien, H.S. Choi, M.Y. Jeong, Fluorescence molecular imaging systems for intraoperative image-guided surgery, Appl Spectrosc Rev, 53 (2018) 349-359.

[19] S.L. Troyan, V. Kianzad, S.L. Gibbs-Strauss, S. Gioux, A. Matsui, R. Oketokoun, L. Ngo, A. Khamene, F. Azar, J.V. Frangioni, The FLARE intraoperative near-infrared fluorescence imaging system: a first-in-human clinical trial in breast cancer sentinel lymph node mapping, Ann Surg Oncol, 16 (2009) 2943-2952.

[20] H.S. Choi, S.L. Gibbs, J.H. Lee, S.H. Kim, Y. Ashitate, F. Liu, H. Hyun, G. Park, Y. Xie, S. Bae, M. Henary, J.V. Frangioni, Targeted zwitterionic near-infrared fluorophores for improved optical imaging, Nat Biotechnol, 31 (2013) 148-153.

[21] H. Hyun, M. Henary, T. Gao, L. Narayana, E.A. Owens, J.H. Lee, G. Park, H. Wada, Y. Ashitate, J.V. Frangioni, H.S. Choi, 700-nm zwitterionic near-infrared fluorophores for dual-channel image-guided surgery, Mol Imaging Biol, 18 (2016) 52-61.

[22] Y. Ashitate, A. Levitz, M.H. Park, H. Hyun, V. Venugopal, G. Park, G. El Fakhri, M. Henary, S. Gioux, J.V. Frangioni, H.S. Choi, Endocrine-specific NIR fluorophores for adrenal gland targeting, Chem Commun (Camb), 52 (2016) 10305-10308.

[23] T. Suda, Transition from video-assisted thoracic surgery to robotic pulmonary surgery, Journal of Visualized Surgery, 3 (2017) 55.

[24] P.K. Nguyen, J. Riegler, J.C. Wu, Stem cell imaging: from bench to bedside, Cell Stem Cell, 14 (2014) 431-444.

[25] K. Hoshino, H.Q. Ly, J.V. Frangioni, R.J. Hajjar, In vivo tracking in cardiac stem cell-based therapy, Prog Cardiovasc Dis, 49 (2007) 414-420.

[26] A. Lopez-Izquierdo, M. Warren, M. Riedel, S. Cho, S. Lai, R.L. Lux, K.W. Spitzer, I.J. Benjamin, M. Tristani-Firouzi, C.J. Jou, A near-infrared fluorescent voltage-sensitive dye allows for moderate-throughput electrophysiological analyses of human induced pluripotent stem cell-derived cardiomyocytes, Am J Physiol Heart Circ Physiol, 307 (2014) H1370-1377.

[27] M.L. Chang Liao, T.P. de Boer, H. Mutoh, N. Raad, C. Richter, E. Wagner, B.R. Downie, B. Unsold, I. Arooj, K. Streckfuss-Bomeke, S. Doker, S. Luther, K. Guan, S. Wagner, S.E. Lehnart, L.S. Maier, W. Stuhmer, E. Wettwer, T. van Veen, M.M. Morlock, T. Knopfel, W.H. Zimmermann, sensing cardiac electrical activity with a cardiac myocyte--targeted optogenetic voltage indicator, Circ Res, 117 (2015) 401-412.

[28] A.V. Naumova, M. Modo, A. Moore, C.E. Murry, J.A. Frank, Clinical imaging in regenerative medicine, Nat Biotechnol, 32 (2014) 804-818.

[29] R. Langer, J.P. Vacanti, Tissue engineering, Science, 260 (1993) 920-926.

[30] A. Atala, Tissue engineering and regenerative medicine: concepts for clinical application, Rejuvenation Res, 7 (2004) 15-31.

[31] E.S. Place, N.D. Evans, M.M. Stevens, Complexity in biomaterials for tissue engineering, Nature materials, 8 (2009) 457-470.

[32] D.W. Hutmacher, Scaffolds in tissue engineering bone and cartilage, Biomaterials, 21 (2000) 2529-2543.

[33] N. Artzi, N. Oliva, C. Puron, S. Shitreet, S. Artzi, A. bon Ramos, A. Groothuis, G. Sahagian, E.R. Edelman, In vivo and in vitro tracking of erosion in biodegradable materials using non-invasive

fluorescence imaging, Nat Mater, 10 (2011) 704-709.

[34] B.K. Kim, Y.H. Ahn, J.J. Kim, M.S. Choi, M.H. Bae, K. Kang, J.S. Lim, R. Lopez, N. Kim, Transport measurement of Andreev bound states in a Kondo-correlated quantum dot, Phys Rev Lett, 110 (2013) 076803.

[35] S.H. Kim, J.H. Lee, H. Hyun, Y. Ashitate, G. Park, K. Robichaud, E. Lunsford, S.J. Lee, G. Khang, H.S. Choi, Near-infrared fluorescence imaging for noninvasive trafficking of scaffold degradation, Sci Rep, 3 (2013) 1198.

[36] E.J. Akins, P. Dubey, Noninvasive imaging of cell-mediated therapy for treatment of cancer, Journal of nuclear medicine : official publication, Society of Nuclear Medicine, 49 Suppl 2 (2008) 180S-195S.

[37] G.K. Park, s. Hoseok, G.S. Kim, N.S. Hwang, H.S. Choi, Optical spectroscopic imaging for cell therapy and tissue engineering, Appl Spectrosc Rev, 53 (2018) 360-375.

[38] F.D. Pagani, H. DerSimonian, A. Zawadzka, K. Wetzel, A.S. Edge, D.B. Jacoby, J.H. Dinsmore, S. Wright, T.H. Aretz, H.J. Eisen, K.D. Aaronson, Autologous skeletal myoblasts transplanted to ischemia-damaged myocardium in humans. Histological analysis of cell survival and differentiation, J Am Coll Cardiol, 41 (2003) 879-888.

[39] J.H. Lee, G. Park, G.H. Hong, J. Choi, H.S. Choi, Design considerations for targeted optical contrast agents, Quant Imaging Med Surg, 2 (2012) 266-273.

[40] H.S. Choi, W. Liu, P. Misra, E. Tanaka, J.P. Zimmer, B. Itty Ipe, M.G. Bawendi, J.V. Frangioni, Renal clearance of quantum dots, Nat Biotechnol, 25 (2007) 1165-1170.

[41] R.G. Blasberg, J. Gelovani, Molecular-genetic imaging: a nuclear medicine-based perspective, Mol Imaging, 1 (2002) 280-300.

[42] S. Arnhold, D. Lenartz, K. Kruttwig, F.J. Klinz, E. Kolossov, J. Hescheler, V. Sturm, C. Andressen, K. Addicks, Differentiation of green fluorescent protein-labeled embryonic stem cell-derived neural precursor cells into Thy-1-positive neurons and glia after transplantation into adult rat striatum, J Neurosurg, 93 (2000) 1026-1032.

[43] L. Dong, X. Zhang, C. Yu, T. Yu, S. Liu, L. Hou, L. Fu, S. Yi, W. Chen, Monitoring luciferase-labeled human prostate stem cell antigen-expressing tumor growth in a mouse model, Exp Ther Med, 6 (2013) 1208-1212.

[44] F. Hu, B. Liu, Organelle-specific bioprobes based on fluorogens with aggregation-induced emission (AIE) characteristics, Org Biomol Chem, 14 (2016) 9931-9944.

[45] L.D. Frye, M. Edidin, The rapid intermixing of cell surface antigens after formation of mouse-human heterokaryons, J Cell Sci, 7 (1970) 319-335.

[46] C. De Duve, R. Wattiaux, Functions of lysosomes, Annu Rev Physiol, 28 (1966) 435-492.

[47] H.S. Choi, K. Nasr, S. Alyabyev, D. Feith, J.H. Lee, S.H. Kim, Y. Ashitate, H. Hyun, G. Patonay, L. Strekowski, M. Henary, J.V. Frangioni, Synthesis and in vivo fate of zwitterionic near-infrared fluorophores, Angew Chem Int Ed Engl, 50 (2011) 6258-6263.

[48] H. Hyun, E.A. Owens, L. Narayana, H. Wada, J. Gravier, K. Bao, J.V. Frangioni, H.S. Choi, M. Henary, Central C-C bonding increases optical and chemical stability of NIR fluorophores, RSC Adv, 4 (2014) 58762-58768.

[49] C.N. Njiojob, E.A. Owens, L. Narayana, H. Hyun, H.S. Choi, M. Henary, Tailored near-infrared contrast agents for image guided surgery, J Med Chem, 58 (2015) 2845-2854.

[50] E.A. Owens, H. Hyun, S.H. Kim, J.H. Lee, G. Park, Y. Ashitate, J. Choi, G.H. Hong, S. Alyabyev, S.J. Lee, G. Khang, M. Henary, H.S. Choi, Highly charged cyanine fluorophores for trafficking scaffold degradation, Biomed Mater, 8 (2013) 014109.

[51] F. Lassailly, E. Griessinger, D. Bonnet, "Microenvironmental contaminations" induced by fluorescent lipophilic dyes used for

noninvasive in vitro and in vivo cell tracking, Blood, 115 (2010) 5347-5354.

[52] F. Kazmi, T. Hensley, C. Pope, R.S. Funk, G.J. Loewen, D.B. Buckley, A. Parkinson, Lysosomal sequestration (trapping) of lipophilic amine (cationic amphiphilic) drugs in immortalized human hepatocytes (Fa2N-4 cells), Drug Metab Dispos, 41 (2013) 897-905.

[53] H.S. Choi, W. Liu, P. Misra, E. Tanaka, J.P. Zimmer, B. Itty Ipe, M.G. Bawendi, J.V. Frangioni, Renal clearance of quantum dots, Nature biotechnology, 25 (2007) 1165-1170.

[54] L. Yuan, L. Wang, B.K. Agrawalla, S.J. Park, H. Zhu, B. Sivaraman, J. Peng, Q.H. Xu, Y.T. Chang, Development of targetable two-photon fluorescent probes to image hypochlorous Acid in mitochondria and lysosome in live cell and inflamed mouse model, J Am Chem Soc, 137 (2015) 5930-5938.

[55] C. Weir, M.C. Morel-Kopp, A. Gill, K. Tinworth, L. Ladd, S.N. Hunyor, C. Ward, Mesenchymal stem cells: isolation, characterisation and in vivo fluorescent dye tracking, Heart Lung Circ, 17 (2008) 395-403.

[56] K.H. Gustavson, Note on the reaction of formaldehyde with collagen, J Biol Chem, 169 (1947) 531-537.

[57] K. Inoue, S.L. Gibbs, F. Liu, J.H. Lee, Y. Xie, Y. Ashitate, H.

Fujii, J.V. Frangioni, H.S. Choi, Microscopic validation of macroscopic in vivo images enabled by same-slide optical and nuclear fusion, J Nucl Med, 55 (2014) 1899-1904.

[58] A. Nakayama, A.C. Bianco, C.Y. Zhang, B.B. Lowell, J.V. Frangioni, Quantitation of brown adipose tissue perfusion in transgenic mice using near-infrared fluorescence imaging, Mol Imaging, 2 (2003) 37-49.

[59] L.B. Chen, Fluorescent labeling of mitochondria, Methods Cell Biol, 29 (1989) 103-123.

[60] M. Terasaki, J. Song, J.R. Wong, M.J. Weiss, L.B. Chen, Localization of endoplasmic reticulum in living and glutaraldehyde-fixed cells with fluorescent dyes, Cell, 38 (1984) 101-108.

[61] A.I. Maas, N. Stocchetti, R. Bullock, Moderate and severe traumatic brain injury in adults, Lancet Neurol, 7 (2008) 728-741.

[62] N.S. Ward, Restoring brain function after stroke - bridging the gap between animals and humans, Nat Rev Neurol, 13 (2017) 244-255.

[63] A.M. Bond, G.L. Ming, H. Song, Adult mammalian neural stem cells and neurogenesis: five decades later, Cell Stem Cell, 17 (2015) 385-395.

[64] S.W. Lane, D.A. Williams, F.M. Watt, Modulating the stem cell niche for tissue regeneration, Nat Biotechnol, 32 (2014) 795-803.

[65] L.R. Nih, S. Gojgini, S.T. Carmichael, T. Segura, Dual-function injectable angiogenic biomaterial for the repair of brain tissue following stroke, Nat Mater, 17 (2018) 642-651.

[66] L.R. Nih, S.T. Carmichael, T. Segura, Hydrogels for brain repair after stroke: an emerging treatment option, Curr Opin Biotechnol, 40 (2016) 155-163.

[67] K.J. Park, T.Y. Jeon, S.Y. Yoo, J.H. Kim, H. Eo, K.D. Song, The appearance of dextranomer-hyaluronic acid copolymer implants on ultrasound may predict resolution of vesicoureteral reflux after injection therapy, Clin Radiol, 69 (2014) 939-944.

[68] G.K. Park, J.H. Lee, A. Levitz, G. El Fakhri, N.S. Hwang, M. Henary, H.S. Choi, Lysosome-targeted bioprobes for sequential cell tracking from macroscopic to microscopic scales, Adv Mater, 31 (2019) 1806216.

[69] K.S. Kim, H. Hyun, J.A. Yang, M.Y. Lee, H. Kim, S.H. Yun, H.S. Choi, S.K. Hahn, Bioimaging of hyaluronate-interferon alpha conjugates using a non-interfering zwitterionic fluorophore, Biomacromolecules, 16 (2015) 3054-3061.

[70] M.E. Gomes, M.T. Rodrigues, R.M.A. Domingues, R.L. Reis, Tissue engineering and regenerative medicine: new trends and directions-a year in review, Tissue Eng Part B Rev, 23 (2017) 211-224.

[71] S. Zhu, B.C. Yung, S. Chandra, G. Niu, A.L. Antaris, X. Chen, Near-infrared-II (NIR-II) bioimaging via off-Peak NIR-I fluorescence emission, Theranostics, 8 (2018) 4141-4151.

[72] S. Zhu, R. Tian, A.L. Antaris, X. Chen, H. Dai, Near-Infrared-II molecular dyes for cancer imaging and surgery, Adv Mater, (2019) 1900321.

[73] S. Hou, Q. Xu, W. Tian, F. Cui, Q. Cai, J. Ma, I.S. Lee, The repair of brain lesion by implantation of hyaluronic acid hydrogels modified with laminin, J Neurosci Methods, 148 (2005) 60-70.

[74] S.H. Kim, S.H. Lee, J.E. Lee, S.J. Park, K. Kim, I.S. Kim, Y.S. Lee, N.S. Hwang, B.G. Kim, Tissue adhesive, rapid forming, and sprayable ECM hydrogel via recombinant tyrosinase crosslinking, Biomaterials, 178 (2018) 401-412.

[75] B.P. Pandey, N. Lee, B.G. Kim, Effect of Extracellular tyrosinase on the expression level of P450, Fpr, and Fdx and ortho-hydroxylation of Daidzein in Streptomyces avermitilis, Appl Biochem Biotechnol, 184 (2018) 1036-1046.

[76] M. Hintersteiner, A. Enz, P. Frey, A.L. Jaton, W. Kinzy, R. Kneuer, U. Neumann, M. Rudin, M. Staufenbiel, M. Stoeckli, K.H. Wiederhold, H.U. Gremlich, In vivo detection of amyloid-beta deposits by near-infrared imaging using an oxazine-derivative probe, Nat Biotechnol, 23 (2005) 577-583.

[77] N.D. Leipzig, M.S. Shoichet, The effect of substrate stiffness on adult neural stem cell behavior, Biomaterials, 30 (2009) 6867-6878.

[78] A.R. Massensini, H. Ghuman, L.T. Saldin, C.J. Medberry, T.J. Keane, F.J. Nicholls, S.S. Velankar, S.F. Badylak, M. Modo, Concentration-dependent rheological properties of ECM hydrogel for intracerebral delivery to a stroke cavity, Acta Biomater, 27 (2015) 116-130.

[79] B. Rashid, M. Destrade, M.D. Gilchrist, Mechanical characterization of brain tissue in compression at dynamic strain rates, J Mech Behav Biomed Mater, 10 (2012) 23-38.

[80] Z. Taylor, K. Miller, Reassessment of brain elasticity for analysis of biomechanisms of hydrocephalus, J Biomech, 37 (2004) 1263-1269.

[81] S. Budday, R. Nay, R. de Rooij, P. Steinmann, T. Wyrobek, T.C. Ovaert, E. Kuhl, Mechanical properties of gray and white matter brain tissue by indentation, J Mech Behav Biomed Mater, 46 (2015) 318-330.

[82] N. Antonovaite, S.V. Beekmans, E.M. Hol, W.J. Wadman, D. Iannuzzi, Regional variations in stiffness in live mouse brain tissue determined by depth-controlled indentation mapping, Sci Rep, 8 (2018) 12517.

[83] Y. Liang, A. Bar-Shir, X. Song, A.A. Gilad, P. Walczak, J.W. Bulte, Label-free imaging of gelatin-containing hydrogel scaffolds, Biomaterials, 42 (2015) 144-150.

[84] O. Aktas, O. Ullrich, C. Infante-Duarte, R. Nitsch, F. Zipp, Neuronal damage in brain inflammation, Arch Neurol, 64 (2007) 185-189.

[85] G. Lucignani, M. Rodriguez-Porcel, In vivo imaging for stem cell therapy: new developments and future challenges, Eur J Nucl Med Mol Imaging, 38 (2011) 400-405.

[86] J.C. Wu, M.R. Abraham, D.L. Kraitchman, Current perspectives on imaging cardiac stem cell therapy, J Nucl Med, 51 Suppl 1 (2010) 128S-136S.

[87] F.J. Nicholls, W. Ling, G. Ferrauto, S. Aime, M. Modo, Simultaneous MR imaging for tissue engineering in a rat model of stroke, Scientific reports, 5 (2015) 14597.

[88] Y. Li, Y. Yao, Z. Sheng, Y. Yang, G. Ma, Dual-modal tracking of transplanted mesenchymal stem cells after myocardial infarction, Int J Nanomedicine, 6 (2011) 815-823.

[89] J. Cao, X. Li, N. Chang, Y. Wang, J. Lei, D. Zhao, K. Gao, Z. Jin, Dual-modular molecular imaging to trace transplanted bone mesenchymal stromal cells in an acute myocardial infarction model, Cytotherapy, 17 (2015) 1365-1373.

[90] S. Gioux, V. Kianzad, R. Ciocan, H.S. Choi, C. Nelson, J. Thumm, R.J. Filkins, S.J. Lomnes, J.V. Frangioni, A low-cost, linear, DC - 35 MHz, high-power LED driver for continuous wave (CW) and fluorescence lifetime imaging (FLIM), Proc Soc Photo Opt Instrum Eng, 6848 (2008) 684807.

[91] C.L. Hutchinson, J.R. Lakowicz, E.M. Sevick-Muraca, Fluorescence lifetime-based sensing in tissues: a computational study, Biophys J, 68 (1995) 1574-1582.

[92] S. Gioux, S.J. Lomnes, H.S. Choi, J.V. Frangioni, Low-frequency wide-field fluorescence lifetime imaging using a high-power near-infrared light-emitting diode light source, J Biomed Opt, 15 (2010) 026005.

[93] C. Wu, G. Ma, J. Li, K. Zheng, Y. Dang, X. Shi, Y. Sun, F. Li, Z. Zhu, In vivo cell tracking via (1)(8)F-fluorodeoxyglucose labeling: a review of the preclinical and clinical applications in cell-based diagnosis and therapy, Clin Imaging, 37 (2013) 28-36.

[94] H.H. Wu, E. Bellmunt, J.L. Scheib, V. Venegas, C. Burkert, L.F. Reichardt, Z. Zhou, I. Farinas, B.D. Carter, Glial precursors clear sensory neuron corpses during development via Jedi-1, an engulfment receptor, Nat Neurosci, 12 (2009) 1534-1541.

[95] C. Kim, C. Favazza, L.V. Wang, In vivo photoacoustic tomography of chemicals: high-resolution functional and molecular

optical imaging at new depths, Chem Rev, 110 (2010) 2756-2782.

[96] L.V. Wang, S. Hu, Photoacoustic tomography: in vivo imaging from organelles to organs, Science, 335 (2012) 1458-1462.

[97] W.K. Yang, C.K. Kang, A.D. Hsu, C.H. Lin, T.H. Lee, Different modulatory mechanisms of renal FXYD12 for Na(+)-K(+)-ATPase between two closely related medakas upon salinity challenge, Int J Biol Sci, 12 (2016) 730-745.

[98] A. Hackethal, M. Hirschburger, S.O. Eicker, T. Mucke, C. Lindner, O. Buchweitz, Role of indocyanine green in fluorescence imaging with near-infrared light to identify sentinel lymph nodes, lymphatic vessels and pathways prior to surgery - A critical evaluation of options, Geburtshilfe Frauenheilkd, 78 (2018) 54-62.

[99] G. Hong, J.C. Lee, J.T. Robinson, U. Raaz, L. Xie, N.F. Huang, J.P. Cooke, H. Dai, Multifunctional in vivo vascular imaging using near-infrared II fluorescence, Nat Med, 18 (2012) 1841-1846.

[100] A. Haque, M.S.H. Faizi, J.A. Rather, M.S. Khan, Next generation NIR fluorophores for tumor imaging and fluorescence-guided surgery: A review, Bioorg Med Chem, 25 (2017) 2017-2034.

요약(국문초록)

조직재생 추적을 위한 세포 분자 영상 기법

의학의 발전과 함께 세포를 이용한 재생의학 및 난치성 질병 치료의 연구가 활발히 이루어지고 있다. 일반적으로 질병이나 사고, 혹은 노령화 등으로 손상된 심장, 뇌, 척추신경 등의 조직과 장기는 자가 재생능력이 부족하여 일반적인 치료 및 수술을 통한 기능복원이 어려운 것이 현실이다. 즉, 한번 손상된 조직은 그 기능을 잃어버리게 되고, 이때에는 기존 약물치료나 수술을 통한 기능복원이 불가능하다. 최근에는 이를 극복하기 위해 다분화능을 가진 다양한 줄기세포 또는 스캐폴드(scaffold)를 이용, 재생이 어려운 장기를 복원시키거나 난치성 질병 치료에 관한 연구가 활발히 이루어지고 있다.

현재 다양한 치료 기술이 개발되어 그 효능평가 및 안전성 검증에 대한 연구가 이루어지고 있지만, 세포 치료제를 임상에 적용하려면 인체에 주입한 후 일어나는 일련의 현상들을 자세히 관찰할 수 있어야 한다. 특히, 분자 영상 기술을 이용하여 체내에 투여된 세포들과 주변 세포들의 거동을 영상화하고 정량화 할 수 있다면 치료제의 임상적용을 더욱 촉진시킬 수 있을 것이다.

앞서 기술한 효능평가 및 안전성 검증과 관련된 문제를 해결하기 위한 본 논문의 첫 번째 연구내용은 세포 라이소좀(lysosome)을 타깃하는 근적외선 형광 조영제를 개발하여 체내에 투여된 세포를 장시간 관찰하는 것이며, 이에 성공하였다. 다음 연구내용으로는 뇌를

특이적으로 목표하여 실시간 이미징을 가능하게 하는 조영제를 개발함이다. 일반적으로 뇌는 자가재생이 어려운 장기로서 뇌 손상이 생기게 되면 영구적인 장애를 가질 수 있는 바, 본 연구에서는 뇌 특이적 조영제를 이용, 뇌 조직 손상/재생 및 스캐폴드(scaffold) 마모속도를 서로 다른 두 가지 파장을 내는 형광 물질을 활용하여 다중채널 이미징을 함으로써 그 치료과정을 육안으로 쉽게 구분이 가능하게 하였다. 이번 연구는 기존 저해상도 초음파나 MRI를 이용한 영상기법과 달리, 조직 특이적으로 시각화 하였고, 이는 특정 생체 조직들의 맞춤형 표적영상화 가능성을 높일 수 있을 것이라고 생각된다. 따라서, 본 논문에서는 제시한 '조직재생 추적 기술' 및 '독립형 다중영상 시스템' 은 조직재생 추적뿐만 아니라 정상/손상조직 모사체 개발, 진단의학을 위한 플랫폼 구축, 신약개발 등의 신의료기술 연구에 응용될 가능성이 높다고 판단된다.

주요어: Optical Imaging, Near-infrared, Regenerative Medicine, Cell Tracking, Multichannel Imaging

학번: 2016-30276

Acknowledgment

I would like to thank my advisors, Prof. Nathaniel Hwang and Prof. Hak Soo Choi, for their continuous support and encouragements. This dissertation would not have been possible without their guidance and motivation for teaching, their insightful comments always helped me to move forward with my research projects.

I would also like to extend my sincere gratitude to my thesis committee: Prof. Paik Seung. R., Pro. Kim Byung-Soo, Prof. Son Kuk Hui, and Prof. Kim Soon Hee for their comments and questions to widen my research from various perspectives.

Lastly and most importantly, I would like to give a special thanks to my family and friends for their love and support throughout my life.

I am very thankful and grateful for all the experiences I have gained during my doctoral studies. Last few years have been challenging time of my life, but at the same time I have grown academically and personally. I firmly believe that knowledge of all aspects I have gained through graduate study will enable me to make greater contributions to the field of bioengineering and the health of society at-large.

~ Kate Park '19